

# A Characteristic Mapping Method for Tracer Transport on the Sphere

Seth Taylor<sup>a,\*</sup>, Jean-Christophe Nave<sup>a</sup>

<sup>a</sup>*Department of Mathematics and Statistics, McGill University, Montréal, Québec H3A 0B9, Canada*

---

## Abstract

A semi-Lagrangian Characteristic Mapping method for the solution of the tracer transport equations on the sphere is presented. The method solves for the solution operator of the equations by approximating the inverse of the diffeomorphism generated by a given velocity field. The evolution of any tracer and mass density can then be computed via pullback with this map. We present a novel spatial discretization of the manifold-valued map using a projection-based approach with spherical spline interpolation. The numerical scheme yields  $C^1$  continuity for the map and global second-order accuracy for the solution of the tracer transport equations. Error estimates are provided and supported by convergence tests involving solid body rotation, moving vortices, deformational, and compressible flows. Additionally, we illustrate some unique features of computing the solution operator using a numerical mixing test and the transport of a fractal set in a complex flow environment.

**Keywords:** Tracer Transport, Manifold-Valued Data, Arbitrary Resolution, Characteristic Mapping Method, Gradient-Augmented Level-Set Method

---

## 1. Introduction

Numerical simulations of transport phenomena on the sphere are an indispensable tool in atmospheric and climate modeling. Modern atmospheric and chemistry-transport models aim to simulate the transport of a large number of tracer species over long periods of time [1, 2], often carrying subgrid information with them [3]. The predictive power and veracity of these simulations can be limited by the associated computational costs [4, 5]. In this paper, we introduce a novel numerical framework, the Characteristic Mapping (CM) method, that possesses a number of desirable features related to this problem. Specifically, the method is able to retain all spatial scales in a transported quantity and coherently transport an arbitrarily large number of quantities. These features are a consequence of directly computing the evolution of the backward characteristic map generated by the velocity field; providing a solution operator to the tracer transport equations. As a result, this mitigates the necessity of discretizing the advected tracer and density and permits their transport via pullback with a *single* numerically approximated backward characteristic map.

Existing numerical methods for the transport equation aim to compute the evolution of the advected quantity using the Eulerian, Lagrangian or semi-Lagrangian frameworks. An Eulerian scheme employs a spatial discretization on a static grid, allowing for ease of access to the solution and an easily parallelizable implementation. However, representing the solution on a static grid comes at the cost of time-stepping restrictions imposed by the Courant-Friedrichs-Lewy condition. In an effort to resolve fine-scale features, adaptive techniques have been developed [6, 7, 8]. Lagrangian schemes alleviate these restrictions by following particle trajectories in the flow. The resulting solutions are generally less prone to numerical dissipation and have better stability properties [9]. A well-known difficulty arising in Lagrangian schemes is that an initially well-ordered set of points may become increasingly disordered over time [10, 11]. Techniques to avoid excessive distortion include reseeding at regular time intervals [12, 13, 14, 15] and adaptive methods [16, 17]. Another more recent approach, called indirect remeshing, interpolates the inverse flow map for the Lagrangian trajectories and then re-samples the initial advected quantity [18, 19, 20]. Finally, the semi-Lagrangian (SL)

---

\*Corresponding author

Email address: [seth.taylor@mail.mcgill.ca](mailto:seth.taylor@mail.mcgill.ca) (Seth Taylor)

framework maintains a spatial discretization using an Eulerian grid while computing the evolution in the Lagrangian frame. Specifically, characteristics are traced back in time and the advected quantity is updated via interpolation. Related approaches include the Arbitrary Lagrangian-Eulerian method [21], particle-mesh methods [22, 23], flux-form [24] and more recent hybrid schemes [25, 26, 27]. Furthermore, conservative SL schemes have been developed and successfully applied for transport on the sphere [28, 29].

Other popular SL schemes for the linear advection of sets and surfaces are Level-Set methods [30]. Higher order accuracy may be generated within these methods by additionally transporting gradient information of the solution [31, 32, 33]. For quantities containing sub-grid features or for sets with poor regularity, the transport of gradient information may be infeasible. Recently, the CM method was developed to address this problem by Mercier et al. [34] for the linear transport of arbitrary sets in two and three dimensional periodic domains. The CM method directly computes the evolution of the backward characteristic map generated by the velocity field. In turn, this provides a discrete approximation of the solution operator to the advection equation, given by the pullback of the initial condition with the backward characteristic map. Multiple quantities may be transported simultaneously from a single numerically approximated flow-map. The accurate tracking of these quantities is determined by the accuracy at which the map is computed. Nevertheless, since the initial condition need not be discretized, the method possesses the capability of representing arbitrarily fine features. This work was further extended to solve the incompressible Euler equations by Yin et al. [35, 36] in the same geometry.

The methods developed in [34, 35, 36] utilized an intrinsic spatial discretization of the map in an angular coordinate system. This in turn permitted the use of classical interpolation techniques relying upon an underlying vector space structure. The geometry of the sphere complicates this intrinsic approach due to the need of multiple overlapping coordinate charts. In this work, we instead consider an extrinsic formulation for the spatial discretization of the backward characteristic map using a projection-based interpolation framework for manifold-valued data. More specifically, we utilize a vector-valued spherical spline interpolant combined with a projection onto the sphere to obtain a  $C^1$  approximation the backward characteristic map.

The paper is organized as follows: section 2 begins with the mathematical formulation of the CM method for the solution of the tracer transport equations. Section 3 details the numerical implementation, outlining the spatial discretization via quadratic spline interpolation on the Powell-Sabin split along with the time evolution using the GALS method. Thereafter, we provide error estimates supported by convergence tests for four standard test cases involving a variety of flow environments in section 4. Finally, we conclude with a presentation of some unique features of the method by a zoom-in on the solution for the transport of a fractal set in a complex flow environment.

## 2. Mathematical Formulation

In this section we outline the mathematical formulation of the CM method for tracer transport on a surface  $\mathcal{S} \subset \mathbb{R}^3$ . We first describe the governing equations and solution strategy for the backward characteristic map as developed in [34, 35], adapted here for the geometry of  $\mathcal{S}$ . Thereafter, we demonstrate how the map may be associated with a solution operator for the transport equations.

### 2.1. The Backward Characteristic Map

Let  $\text{Diff}(\mathcal{S})$  be the space of diffeomorphisms of  $\mathcal{S}$ . The central object of interest in the CM method is the family of diffeomorphisms  $\mathbf{X}_{[t,s]} \in \text{Diff}(\mathcal{S})$  generated by a velocity field  $\mathbf{u} : \mathcal{S} \times \mathbb{R} \rightarrow T\mathcal{S}$  over an interval of time  $[t, s]$ . We call these diffeomorphisms the characteristic maps as they provide a solution operator to the ordinary differential equation

$$\dot{\gamma}(t) = \mathbf{u}(\gamma(t), t), \quad \gamma(s) = \mathbf{x}, \quad (2.1)$$

for characteristic curves  $\gamma : \mathbb{R} \rightarrow \mathcal{S}$  parameterized by the initial condition  $\mathbf{x} \in \mathcal{S}$ . Fixing  $s = t_0 < t$ , we define the forward characteristic map  $\mathbf{X}_{[t_0,t]} : \mathcal{S} \times \mathbb{R} \rightarrow \mathcal{S}$  as the solution operator to (2.1) and the backward characteristic map  $\mathbf{X}_{[t,t_0]}$  as the inverse of  $\mathbf{X}_{[t_0,t]}$ , that is

$$\mathbf{X}_{[t,t_0]} \circ \mathbf{X}_{[t_0,t]} = \text{id}_{\mathcal{S}}. \quad (2.2)$$

The backward characteristic map provides a solution operator to (2.1) backwards in time. Differentiating the expression (2.2) with respect to time we get that  $\mathbf{X}_{[t,t_0]}$  satisfies an initial value problem of the form

$$\begin{aligned}\partial_t \mathbf{X}_{[t,t_0]} + d\mathbf{X}_{[t,t_0]}(\mathbf{u}) &= 0, \\ \mathbf{X}_{[t_0,t_0]} &= \text{id}_{\mathcal{S}}.\end{aligned}\tag{2.3}$$

where  $d\mathbf{X}_{[t,t_0]} : T\mathcal{S} \rightarrow T\mathcal{S}$  is the differential (pushforward) of the backward characteristic map. The CM method utilizes the semi-group structure of the characteristic map to compute the solution to (2.3). Consider partitioning an interval of time into  $m$  subdivisions  $[t_i, t_{i+1}] \subset [0, T]$  for  $i \in \{0, 1, \dots, m-1\}$ . We may decompose  $\mathbf{X}_{[T,0]}$  into a set of submaps  $\mathbf{X}_{[t_{i+1},t_i]} : \mathcal{S} \rightarrow \mathcal{S}$  (defined in [35]), determined by the solutions of the following initial value problems

$$\partial_t \mathbf{X}_{[t_{i+1},t_i]}(\mathbf{x}) + d\mathbf{X}_{[t_{i+1},t_i]}(\mathbf{u}) = 0, \quad \mathbf{X}_{[t_{i+1},t_{i+1}]} = \mathbf{x},\tag{2.4}$$

backward in time to time  $t_i$ . Using the semigroup property, the backward characteristic map to time  $T$  is then obtained via composition of each submap, that is

$$\mathbf{X}_{[T,0]}(\mathbf{x}) = \mathbf{X}_{[t_1,0]} \circ \mathbf{X}_{[t_1,t_2]} \cdots \circ \mathbf{X}_{[t_m,t_{m-1}]}(\mathbf{x}).\tag{2.5}$$

We note that this formulation is geometrically intrinsic and holds without the need for a Riemannian metric structure on the surface.

## 2.2. Transport Equations

The equations governing the evolution of a tracer mixing ratio  $\phi$  and fluid density  $\rho$  transported by a given velocity field  $\mathbf{u}$  in the absence of sources or sinks are given by

$$\partial_t \rho + \nabla_{\mathcal{S}} \cdot (\rho \mathbf{u}) = 0, \quad \rho(\mathbf{x}, 0) = \rho_0,\tag{2.6a}$$

$$\partial_t (\rho \phi) + \nabla_{\mathcal{S}} \cdot (\rho \phi \mathbf{u}) = 0, \quad \phi_0(\mathbf{x}, 0) = \phi_0,\tag{2.6b}$$

where  $\nabla_{\mathcal{S}} \cdot$  is the surface divergence operator and  $\phi_0, \rho_0$  are the initial conditions. Let  $U_0 \subseteq \mathcal{S}$  be a fixed reference configuration in the fluid such that  $U(t) = \mathbf{X}_{[0,t]}(U_0)$  and let  $\mathbf{X}_{[0,t]}(\mathbf{x}) = \boldsymbol{\alpha} \in U(t)$  be the Lagrangian particle position with position  $\mathbf{x} \in U_0$  in the Eulerian frame. In integral form, the continuity equations (2.6) can be expressed as a coupled set of conservation laws

$$\frac{d}{dt} \int_{U(t)} \rho(\boldsymbol{\alpha}, t) \mu(\boldsymbol{\alpha}) = 0,\tag{2.7a}$$

$$\frac{d}{dt} \int_{U(t)} \rho(\boldsymbol{\alpha}, t) \phi(\boldsymbol{\alpha}, t) \mu(\boldsymbol{\alpha}) = 0,\tag{2.7b}$$

where  $\mu \in \Omega^2(\mathcal{S})$  is a volume form. By a change of variables with the backward characteristic map, conservation of mass (2.7a) gives us that

$$\int_{U(t)} \rho(\boldsymbol{\alpha}, t) \mu(\boldsymbol{\alpha}) = \int_{U_0} \rho_0(\mathbf{x}) \mu(\mathbf{x}) = \int_{U(t)} \mathbf{X}_{[t,0]}^* (\rho_0 \mu) = \int_{U(t)} \rho_0 \circ \mathbf{X}_{[t,0]}(\boldsymbol{\alpha}) J_{\mu}(\mathbf{X}_{[t,0]})(\boldsymbol{\alpha}) \mu(\boldsymbol{\alpha}).\tag{2.8}$$

where  $J_{\mu}(\mathbf{X}_{[t,0]}) \in C^{\infty}(\mathcal{S})$  is the Jacobian determinant with respect to  $\mu$  of the backward characteristic map. Since  $\rho_0$  is well-defined and  $U_0$  is arbitrary, we get that the solution to (2.6a) is given by

$$\rho(\mathbf{x}, t) = (\rho_0 \circ \mathbf{X}_{[t,0]}) J_{\mu}(\mathbf{X}_{[t,0]})(\mathbf{x}), \quad \forall (\mathbf{x}, t) \in \mathcal{S} \times \mathbb{R}_+\tag{2.9}$$

Using a similar change of variables as in (2.8) for the tracer density conservation (2.7b) and applying (2.9) we get that the evolution of the tracer mixing ratio is governed by

$$\phi(\mathbf{x}, t) = \phi_0 \circ \mathbf{X}_{[t,0]}(\mathbf{x}), \quad \forall (\mathbf{x}, t) \in \mathcal{S} \times \mathbb{R}_+.\tag{2.10}$$

Using the relations (2.9) and (2.10), we see that  $\mathbf{X}_{[t,0]}$  defines a solution operator to the transport equations (2.6) by pullback

$$\mathbf{X}_{[t,0]}^* : \mathcal{F}(\mathcal{S}) \times \text{Dens}(\mathcal{S}) \rightarrow \mathcal{F}(\mathcal{S}) \times \text{Dens}(\mathcal{S}), \quad (\phi_0, \rho_0) \mapsto (\phi_0 \circ \mathbf{X}_{[t,0]}, \rho_0 \circ \mathbf{X}_{[t,0]} J_{\mu}(\mathbf{X}_{[t,0]}))\tag{2.11}$$

where  $\mathcal{F}(\mathcal{S})$  and  $\text{Dens}(\mathcal{S})$  are the spaces of  $\mathbb{R}$ -valued functions and of densities on  $\mathcal{S}$  respectively.

**Remark 1.** The backward characteristic map  $\mathbf{X}_{[t,0]}$  forms a path in the space of diffeomorphisms of  $\mathcal{S}$ . The action defined by (2.11) is the natural group action of  $\text{Diff}(\mathcal{S})$  on the product space  $\mathcal{F}(\mathcal{S}) \times \text{Dens}(\mathcal{S})$ . Furthermore, the action of the diffeomorphism group on the space of  $k$ -forms  $\Omega^k(\mathcal{S})$  is also given by the pullback. Using this action, the backward characteristic map defines a solution operator for the general Lie advection equation on  $k$ -forms. This can be readily observed as follows. Suppose that a family of  $k$ -forms  $\omega(t) \in \Omega^k(\mathcal{S})$  satisfies the initial value problem

$$(\partial_t + \mathcal{L}_{\mathbf{u}})\omega = 0, \quad \omega(0) = \omega_0. \quad (2.12)$$

Then taking the time derivative of the pullback of  $\omega(t)$  with the forward characteristic map we obtain

$$\frac{d}{dt} \mathbf{X}_{[0,t]}^* \omega = \mathbf{X}_{[0,t]}^* (\partial_t \omega + \mathcal{L}_{\mathbf{u}} \omega) = 0 \implies \mathbf{X}_{[0,t]}^* (\omega(t)) = \omega_0 \iff \omega(t) = \mathbf{X}_{[t,0]}^* (\omega_0). \quad (2.13)$$

In the case that the velocity field is incompressible we have that  $J_\mu(\mathbf{X}_{[t,0]}) = 1$ . Moreover, if the initial fluid density is also constant then the evolution of  $\rho\phi$  is governed entirely by (2.10). In the forthcoming numerical tests we will consider an initially constant density fluid and solve for the evolution of  $\rho$  and  $\phi$  using both compressible and incompressible velocity fields.

There are many benefits of solving for the entire solution operator to the transport equations (2.6). A single numerical approximation of the map  $\mathbf{X}_{[t,0]}$  can be used to transport an arbitrary number of quantities at the cost of the composition (2.10). Since the map is the only quantity which necessitates discretization, the formulation permits the transport of quantities with arbitrarily fine spatial scales. Moreover, since the solution operator (2.11) acts on the entire space  $\mathcal{F}(\mathcal{S})$ , the regularity of an advected quantity bears no constraint on its evolution.

### 3. Numerical Framework

In this section we describe the numerical framework for the CM method for the tracer transport equations on the unit sphere centred at the origin, i.e.  $\mathcal{S} = \mathbb{S}^2$ , hereafter referred to as just the sphere. We note that the embedding-based formulation of the method is not limited to the sphere and could be extended to a more general class of manifolds beyond the scope of what is presented here. We begin with a brief description of the solution algorithm and remark upon the discretization of the backward characteristic map in the context of manifold-valued approximation. Let  $t_n > 0$  be time steps with  $t_{n+1} - t_n = \Delta t$  and denote  $\mathcal{X}_{[t,0]}$  as the numerical approximation of  $\mathbf{X}_{[t,0]}$ . The CM approach employs a semi-Lagrangian method to compute the evolution of the backward characteristic map. Each iteration updates the backward characteristic map using a discrete analogue of (2.4) and (2.5):

$$\mathcal{X}_{[t_{n+1}, t_n]}(\mathbf{x}) = \mathcal{R}_{\Delta t}(\mathbf{u}, \mathbf{x}), \quad (3.1a)$$

$$\mathcal{X}_{[t_{n+1}, 0]}(\mathbf{x}) = \mathcal{J}_h[\mathcal{X}_{[t_n, 0]} \circ \mathcal{X}_{[t_{n+1}, t_n]}](\mathbf{x}), \quad (3.1b)$$

which is initialized by setting  $\mathbf{X}_{[0,0]}$  as the identity map. The value of the submap as  $\mathbf{x}$  is computed using a numerical integration scheme  $\mathcal{R}_{\Delta t} : \mathfrak{X}(\mathcal{S} \times \mathbb{R}) \times \mathcal{S} \rightarrow \mathcal{S}$  providing an approximate solution to the ordinary differential equation

$$\dot{\gamma}(t) = \mathbf{u}(\gamma(t), t), \quad \gamma(t_{n+1}) = \mathbf{x}, \quad (3.2)$$

backwards in time to  $t_n$ . The backward characteristic map is updated through composition with the submap followed by a spatial discretization via  $\mathcal{J}_h : C^1(\mathcal{S}, \mathcal{S}) \rightarrow \mathcal{V}_h(\mathcal{S})$  where  $\mathcal{V}_h(\mathcal{S}) \subset C^1(\mathcal{S}, \mathcal{S})$  is a finite dimensional interpolation space. We use the built-in interpolation framework of the Gradient-Augmented Level Set (GALS) method [32] to obtain a higher-order accurate approximation of the backward characteristic map. The GALS method utilizes a local Hermite interpolation operator  $\mathcal{J}_h$  defined on a spatial discretization of  $\mathcal{S}$  to interpolate the transported function values and derivative information at the vertices. This data is supplied approximately by integrating for the footpoints of a compact  $\varepsilon$ -difference stencil [32] about the vertices.

The use of classical interpolation techniques which rely upon an underlying vector space structure are complicated by the non-linear nature of the sphere and the space  $C^1(\mathcal{S}, \mathcal{S})$ . In the intrinsic approach to

this approximation problem, the map is expressed in a local coordinate system where standard interpolation techniques and numerical integration schemes on linear spaces can be applied<sup>1</sup>. The need for multiple coordinate charts necessitates the use of overlapping meshes, such as the Yin-Yang grid [38], along with the blending of interpolants over these grids. In contrast, an extrinsic approach to the problem can be taken by considering  $\mathcal{S}$  as embedded in  $\mathbb{R}^3$  and performing the interpolation or numerical integration scheme in the ambient Euclidean space. The interpolant can be subsequently constrained to the surface through the use of a projection operator. In turn, the extrinsic formulation is void of artificial coordinate singularities and possesses the same order of accuracy as the underlying linear interpolation scheme.

In this work, we consider an embedding-based method for the spatial discretization of the backward characteristic map. The approach taken here is similar in spirit to the projection-based interpolation methods for manifold-valued data [39, 40]. The sphere is discretized using a spherical triangulation allowing for the use of the higher-order accurate spherical spline interpolation methods outlined in [41, 42]. The particular choice of spherical spline space considered consists of the quadratic spherical splines on the Powell-Sabin split. This space permits a globally  $C^1$  interpolant from data consisting only of the function values and surface derivatives at the vertices. The resulting scheme offers computational efficiency, third-order accuracy, and algorithmic simplicity. This spatial discretization of the backward characteristic map is formed by modifying the interpolation operator for a scalar valued function on this space to a vector-valued spherical spline composed with a radial projection onto the sphere. Combining this interpolation technique with a higher-order numerical integration scheme results in a globally second-order accurate approximation of the backward characteristic map.

### 3.1. Spatial Discretization

We consider local spline spaces since they are constructed to be locally supported and globally differentiable; both desirable properties exploited by the GALS framework. The particular choice of local spline space considered here are the quadratic spherical splines on the Powell-Sabin split. We note however that the use of other macro-element interpolation techniques such as those for cubic splines on the Clough-Tocher split or higher degree ( $\geq 4$ ) polynomial splines are viable alternatives. A more comprehensive study of the GALS framework for more general spline spaces of higher degree and smoothness on other manifolds is the subject of current research. We begin by providing details on the particular method of interpolation along with error estimates describing the accuracy of the approximation.

#### 3.1.1. Spherical Spline Interpolation on the Powell-Sabin Split

Spherical analogues of bivariate spline spaces were introduced and studied in [42, 43, 44]. It was shown in [42] that many of the bivariate macro-element techniques for higher order interpolation using splines could be naturally carried over to the sphere using their construction. These techniques provide a powerful computational tool to perform local Hermite interpolation without the need to solve a linear system or construct an explicit basis. We provide a description of the construction and approximation power of the Powell-Sabin spherical spline interpolant from which the spatial discretization of the backward characteristic map is formed.

The sphere is discretized using a spherical triangulation  $\Delta = \{T_i\}_{i=1}^{N_\Delta}$  where  $T_i \subset \mathcal{S}$ , constructed by joining an associated set of vertices  $\mathcal{V} = \{v_i\}_{i=1}^{N_v}$  along spherical arcs such that any two spherical triangles share at most one edge and their union covers the entire sphere. In a spherical triangle  $T \in \Delta$  with vertices  $v_1, v_2, v_3 \in \mathbb{R}^3$ , a local coordinate system is defined using the spherical barycentric coordinates of a point  $\mathbf{v} \in T$ . These are given by  $\mathbf{b}(\mathbf{v}) = (b_1, b_2, b_3) \in \mathbb{R}^3$  such that  $\mathbf{v} = b_1 v_1 + b_2 v_2 + b_3 v_3$  where each coordinate  $b_i$  is determined by Cramer's rule. Nearly all properties of trihedral barycentric coordinates carry over to the spherical case, except that they are not required to add up to one [44]. Let  $\Pi_d(\mathcal{S})$  be the space of homogeneous trivariate polynomials in  $\mathbb{R}^3$  restricted to the sphere, hereafter referred to as the space of spherical polynomials. A local basis for  $\Pi_d(\mathcal{S})$  is given by the polynomials

$$B_{ijk}^d(\mathbf{v}) = \frac{d!}{i!j!k!} b_1^i b_2^j b_3^k, \quad i + j + k = d. \quad (3.3)$$

---

<sup>1</sup>We have implemented a method based on a tensor product of Hermite cubics and a higher Runge-Kutta integration scheme on a latitude-longitude spherical coordinate parametric space. The approach is simple and was observed to be highly accurate for many standard cases from [37], although limited in its scope due to the coordinate system.

A local spherical Bernstein-Bézier (SBB) polynomial in  $T$  is then defined by

$$p(v) = \sum_{i+j+k=d} c_{ijk} B_{ijk}^d(v), \quad (3.4)$$

for coefficients  $c_{ijk} \in \mathbb{R}$ . Efficient evaluation of a spherical polynomial in Bernstein-Bézier form can be performed using deCasteljau's algorithm [41]. The directional derivative of a spherical polynomial  $p \in \Pi_d(\mathcal{S})$  in the direction  $\mathbf{g} \in \mathbb{R}^3$  at the point  $\mathbf{v} \in T$  is given by

$$D_{\mathbf{g}}p(\mathbf{v}) = \mathbf{b}(\mathbf{g}) \cdot \nabla_b p(\mathbf{v}), \quad (3.5)$$

where  $\mathbf{b}(\mathbf{g})$  are the barycentric coordinates of  $\mathbf{g}$  relative to  $T$  and  $\nabla_b$  is the derivative of the spherical polynomial in each barycentric coordinate [42]. We note that  $\nabla p(\mathbf{v})$  is defined with respect to the homogeneous Bernstein-Bézier polynomial for which  $p$  is the restriction to the sphere.

The space of spherical splines of smoothness  $r$  and degree  $d$  on  $\Delta$  is defined by [44]:

$$S_d^r(\Delta) = \{s \in C^r(\mathcal{S}) : s|_{T_i} \in \Pi_d(\mathcal{S}) \quad \forall T_i \in \Delta\}. \quad (3.6)$$

In order to obtain full approximation power for an interpolatory spline of degree  $d < 3r + 2$ , the technique of subdivision must be used [41]. In the case  $d = 2$ , one can consider the Powell-Sabin (PS) split, originally introduced for bivariate spline interpolation on planar triangulations [45]. This particular subdivision is formed by joining the vertices and midpoints of each edge to the center of the triangle, resulting in six triangles associated with each macro-triangle  $T$  (see left panel of figure 1). Let  $\Delta_{PS}$  denote the PS refinement of  $\Delta$  and let  $\mathbf{e}_i, \mathbf{e}_{i+1} \in \mathbb{R}^3$  denote the normalized tangent vectors pointing along the edges connected to a vertex  $\mathbf{v}_i$ . It was shown in [42] that for every  $f \in C^1(\mathcal{S})$  there exists a unique spline  $s \in S_2^1(\Delta_{PS})$  satisfying the Hermite interpolation problem

$$s(\mathbf{v}_i) = f(\mathbf{v}_i), \quad D_{\mathbf{e}_i} s(\mathbf{v}_i) = D_{\mathbf{e}_i} f(\mathbf{v}_i), \quad D_{\mathbf{e}_{i+1}} s(\mathbf{v}_i) = D_{\mathbf{e}_{i+1}} f(\mathbf{v}_i), \quad \forall \mathbf{v}_i \in \mathcal{V}. \quad (3.7)$$

These 9 pieces of data are combined with the  $C^1$  continuity conditions across the edges of the subdivision to map into the space  $S_2^1(\Delta_{PS})$  as a set of 19 coefficients for each macro-triangle  $T$ . The evaluation of a spline defined on the PS-split at a point  $\mathbf{v} \in \mathcal{S}$  is performed by first determining the macro-triangle  $T$  through a containing simplex querying strategy. Then, using the barycentric coordinates of  $\mathbf{v}$  relative to  $T$  one can determine in which subdivided triangle the point  $\mathbf{v}$  is contained. The barycentric coordinates of  $\mathbf{v}$  are then computed relative to the sub-triangle and a quadratic SBB polynomial is evaluating using the 6 out of the 19 coefficients which are associated with the sub-triangle 1. Further details on the explicit construction of  $s$  and formulas for the 19 coefficients can be found in [41, 46, 42].

Let  $|T_i|$  be the maximum angular distance between any two points in  $T_i$ , and let  $h = \max\{|T_i|\}$ . The interpolation operator defined by (3.7)

$$\mathcal{I}_h : C^1(\mathcal{S}) \rightarrow S_2^1(\Delta_{PS}) \quad (3.8)$$

satisfies the following error estimate [47, 46]:

$$\|f - \mathcal{I}_h[f]\|_{C(\mathcal{S})} \leq Kh^{m+1} \|f\|_{C^{m+1}(\mathcal{S})}, \quad \forall f \in C^{m+1}(\mathcal{S}) \quad (3.9)$$

where  $0 \leq m \leq 2$  and the constant  $K$  depends on the smallest angle in the triangulation. Moreover, for any  $\mathbf{g} \in T\mathcal{S}$  the directional derivative of the interpolant satisfies

$$\|D_{\mathbf{g}}(f - \mathcal{I}_h[f])\|_{C(\mathcal{S})} \leq Kh^m \|f\|_{C^{m+1}(\mathcal{S})}. \quad (3.10)$$

### 3.1.2. Projection-Based Spline Interpolation

We now modify the spherical spline interpolation to interpolate a map  $\mathbf{X} : \mathcal{S} \rightarrow \mathcal{S}$ . The vector-valued interpolation operator of a map  $\mathbf{X} = (X_1, X_2, X_3)$ , where  $X_i : \mathcal{S} \rightarrow \mathbb{R}$  for each  $i = 1, 2, 3$ , is defined as

$$\begin{aligned} \mathcal{I}_h^{(3)} : C^1(\mathcal{S}, \mathbb{R}^3) &\rightarrow S_2^1(\Delta_{PS})^3 \\ \mathbf{X} &\mapsto (\mathcal{I}_h(X_1), \mathcal{I}_h(X_2), \mathcal{I}_h(X_3)). \end{aligned} \quad (3.11)$$

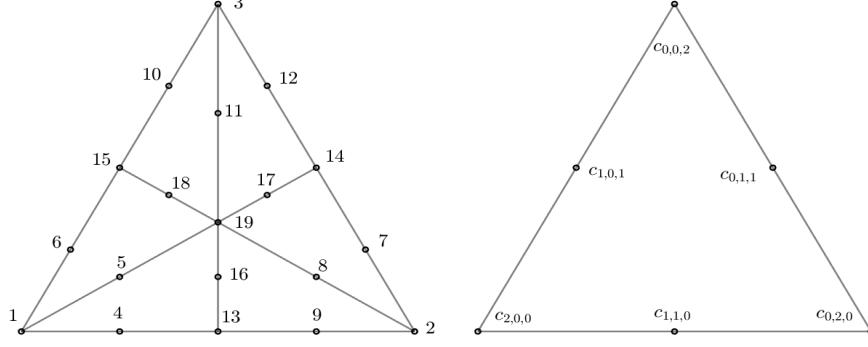


Figure 1: Left: Powell-Sabin split and labelled coefficients. Right: Coefficients associated to quadratic polynomial.

Since the interpolation operator is not constructed to enforce the constraint  $\|\mathcal{I}_h^{(3)}[\mathbf{X}](\mathbf{x})\| = 1$  globally, where  $\|\cdot\|$  is the Euclidean norm in  $\mathbb{R}^3$ , we compensate by composing the operator (3.11) with the radial projection onto the sphere

$$\mathcal{P} : C^1(\mathbb{S}^2, \mathbb{R}^3) \rightarrow C^1(\mathbb{S}^2, \mathbb{S}^2), \quad \mathbf{X} \mapsto \mathbf{X}/\|\mathbf{X}\|. \quad (3.12)$$

The interpolation operator used to define the spatial discretization of the backward characteristic map in (3.1) is thus given by

$$\mathcal{J}_h : C^1(\mathcal{S}, \mathcal{S}) \rightarrow C^1(\mathcal{S}, \mathcal{S}), \quad \mathbf{X} \mapsto \mathcal{P} \circ \mathcal{I}_h^{(3)}[\mathbf{X}]. \quad (3.13)$$

Using this embedding-based approach, the pointwise error is no worse than that of  $\mathcal{I}_h^{(3)}$ , only up to a factor of 2 [39]. This follows from an elementary estimate. Since  $\mathbf{X}(\mathbf{x}) \in \mathcal{S}$ , we have that

$$\begin{aligned} \|\mathcal{J}_h(\mathbf{X})(\mathbf{x}) - \mathbf{X}(\mathbf{x})\| &\leq \|\mathcal{P} \circ \mathcal{I}_h^{(3)}(\mathbf{X})(\mathbf{x}) - \mathcal{I}_h^{(3)}(\mathbf{X})(\mathbf{x})\| + \|\mathbf{X}(\mathbf{x}) - \mathcal{I}_h^{(3)}(\mathbf{X})(\mathbf{x})\| \\ &\leq 2\|\mathbf{X}(\mathbf{x}) - \mathcal{I}_h^{(3)}(\mathbf{X})(\mathbf{x})\|. \end{aligned} \quad (3.14)$$

The differential of (3.13) also satisfies a similar error estimate, but is no longer independent of the geometry of the sphere. We summarize a result on the approximation of the differential proven in [48] for more general manifolds, here in the particular case of the sphere. Let  $\boldsymbol{\xi} = \mathcal{J}_h[\mathbf{X}](\mathbf{x})$  for some  $\mathbf{x} \in \mathcal{S}$  and suppose that  $\mathbf{v} \in T_{\mathbf{x}}\mathcal{S}$ . The differential of (3.13) is given by

$$d\mathcal{J}_h[\mathbf{X}]_{\mathbf{x}} : T_{\mathbf{x}}\mathcal{S} \rightarrow T_{\boldsymbol{\xi}}\mathcal{S}, \quad \mathbf{v} \mapsto d\mathcal{P}_{\boldsymbol{\xi}} \cdot D\mathcal{I}_h^{(3)}[\mathbf{X}](\mathbf{x})\mathbf{v}, \quad (3.15)$$

where  $D\mathcal{I}_h^{(3)}[\mathbf{X}](\mathbf{x})$  is the Jacobian of (3.11) evaluated at  $\mathbf{x}$  using (3.5) and the differential of the projection at  $\boldsymbol{\xi} \in \mathbb{R}^3 \setminus \{0\}$  is given by

$$d\mathcal{P}_{\boldsymbol{\xi}} : \mathbb{R}^3 \rightarrow T_{\boldsymbol{\xi}}\mathcal{S}, \quad \mathbf{v} \mapsto \frac{1}{\|\boldsymbol{\xi}\|} \left( \mathbf{v} - \frac{\langle \boldsymbol{\xi}, \mathbf{v} \rangle}{\|\boldsymbol{\xi}\|^2} \boldsymbol{\xi} \right). \quad (3.16)$$

The error in the differential of a map  $F : \mathcal{S} \rightarrow \mathbb{R}^3$  is measured using the following norm

$$\|dF\|_{2,\infty} := \sup_{\mathbf{x} \in \mathcal{S}} \|dF_{\mathbf{x}}\|_2 \quad (3.17)$$

where  $\|\cdot\|_2$  is the matrix 2-norm. As proven for more general manifolds in [48], if there is a positive constant  $\epsilon < 1$  such that

$$\|\mathbf{X}(\mathbf{x}) - \mathcal{I}_h^{(3)}[\mathbf{X}](\mathbf{x})\| \leq \epsilon, \quad \forall \mathbf{x} \in \mathcal{S}, \quad (3.18)$$

then the approximation of the differential of the map (3.13) satisfies

$$\|d\mathbf{X} - d\mathcal{J}_h[\mathbf{X}]\|_{2,\infty} \leq \|d\mathcal{I}_h^{(3)}[\mathbf{X}] - d\mathbf{X}\|_{2,\infty} + C(\epsilon) \left( \|d\mathcal{I}_h^{(3)}[\mathbf{X}] - d\mathbf{X}\|_{2,\infty} + \|d\mathbf{X}\|_{2,\infty} \right), \quad (3.19)$$

where  $C(\epsilon) = \epsilon(3 - 2\epsilon)(1 - \epsilon)^{-1}$ .

**Remark 2.** In the general setting of embedding-based interpolation methods for manifold-valued data, the pre-asymptotic behaviour of the approximation of the differential is dictated by the reach,  $\tau$ , of the manifold, i.e. the size of the tubular neighbourhood about the embedded submanifold in which the projection is well-defined. A similar estimate to (3.19) holds with the condition that  $\epsilon < \tau$  [48].

### 3.2. The CM Method for Transport on the Sphere

In this section we explain how the interpolation (3.13) and numerical integration schemes in (3.1) are incorporated within the GALS framework to obtain higher-order accuracy. Although the approximation of the characteristic map is constructed such that it takes values in  $\mathbb{R}^3$  the domain is still treated in a more intrinsic manner. To this end, we give a short description of the local tangent plane coordinates used in the analysis of the GALS method on the sphere. We provide error estimates describing the accuracy of the method, yielding a theoretical justification for the results observed in the convergence tests presented in section 4.

#### 3.2.1. Trajectory Computations

The trajectory computations are performed in three-dimensional Cartesian coordinates using a modification of the RK4 numerical integration scheme backwards in time with a projection onto the sphere. Since the ordinary differential equation (2.1) is solved in the embedding space, without the use of a local coordinate system, numerical integration schemes which rely upon additive evolution will not remain on the sphere. Geometric numerical integration schemes have been devised to directly enforce this property [49, 50, 51]. We have considered the fourth-order scheme RKM4 [49] and observed a similar accuracy to the approach taken here. In either case, these techniques do not rely upon an extension of the velocity field into the ambient space. Moreover, for  $\Delta t$  small enough, the radial distance of the trajectory away from the sphere will be of the size of the local error of the integration scheme [52]. Consequently, the accuracy of the trajectory computation will not be compromised through this added projection step.

#### 3.2.2. Local Tangent Plane Coordinates

We give a short description of some properties of this coordinate system. Let  $p \in \mathcal{S}$  and let  $U_p \subset \mathcal{S}$  be an open set such that the projection onto the tangent plane at  $p$  defined by  $\pi_p : U_p \rightarrow T_p\mathcal{S}$  is invertible. Let  $\mathbf{p} \in \mathbb{R}^3$  also denote the normal vector to  $\mathcal{S}$  at  $p$  and let  $\gamma_p^1, \gamma_p^2 \in \mathbb{R}^3$  be unit vectors such that  $\gamma_p^1 \times \gamma_p^2 = \mathbf{p}$ . Regarding  $\mathcal{S}$  and  $T_p\mathcal{S}$  as embedded in  $\mathbb{R}^3$ , then the tangent plane projection can be defined as

$$\pi_p(\mathbf{q}) = \mathbf{p} + \langle \mathbf{q}, \gamma_p^1 \rangle \gamma_p^1 + \langle \mathbf{q}, \gamma_p^2 \rangle \gamma_p^2, \quad \forall \mathbf{q} \in U_p. \quad (3.20)$$

Using a sufficient collection of charts  $\varphi_p : U_p \rightarrow \mathbb{R}^2$  defined by

$$\varphi_p(\mathbf{q}) = (\langle \mathbf{q}, \gamma_p^1 \rangle, \langle \mathbf{q}, \gamma_p^2 \rangle) := (x_1, x_2), \quad (3.21)$$

an atlas for  $\mathcal{S}$  can be formed [47]. In this coordinate system, the metric tensor  $g : T_p\mathcal{S} \times T_p\mathcal{S} \rightarrow \mathbb{R}$  is given by

$$g = (1 - x_1^2 - x_2^2)^{-1} \left( (1 - x_2^2) dx_1^2 + 2x_1x_2 dx_1 dx_2 + (1 - x_1^2) dx_2^2 \right). \quad (3.22)$$

Denote the isomorphisms between the tangent and cotangent planes  $(\cdot)^\flat : T_p\mathcal{S} \rightarrow T_p^*\mathcal{S}$  and  $(\cdot)^\sharp : T_p^*\mathcal{S} \rightarrow T_p\mathcal{S}$  using the metric. The differential of a function  $f : \mathcal{S} \rightarrow \mathbb{R}$  with coordinate representative  $\hat{f} = f \circ \varphi_p^{-1}$  is given by

$$df = \sqrt{\frac{1 - x_1^2 - x_2^2}{1 - x_2^2}} \frac{\partial \hat{f}}{\partial x_1} dx_1 + \sqrt{\frac{1 - x_1^2 - x_2^2}{1 - x_1^2}} \frac{\partial \hat{f}}{\partial x_2} dx_2, \quad (3.23)$$

and the surface gradient of  $f$  is given locally by  $\nabla_{\mathcal{S}} f = (df)^\sharp$ . We will also require the transformation of the gradient of a function expressed in one coordinate system to another. Let  $\zeta, \mu \in \mathcal{S}$  and denote  $\hat{f}_\zeta = f \circ \varphi_\zeta^{-1}$  and let  $\nabla \hat{f}_\zeta(\mu)$  be the gradient of  $\hat{f}_\zeta$  at  $\varphi_\zeta(\mu) \in \varphi_\zeta(U_\zeta)$ . Using the Jacobian of the transition function  $\varphi_\zeta \circ \varphi_\mu^{-1} : \varphi_\mu(U_\mu \cap U_\zeta) \rightarrow \varphi_\zeta(U_\mu \cap U_\zeta)$  at  $\varphi_\mu(\mu)$  given by

$$J_{\zeta, \mu}(\varphi_\mu(\mu)) = [\langle \gamma_\zeta^{(k)}, \gamma_\mu^{(j)} \rangle]_{k,j}, \quad (3.24)$$



the gradient can be transformed to the coordinates system defined by  $\varphi_\mu$  as

$$\nabla \hat{f}_\zeta(\mu) = \nabla \hat{f}_\mu(\mu) J_{\zeta,\mu}(\mu). \quad (3.25)$$

### 3.2.3. Gradient-Augmented Level Set on the Sphere

In the GALs method, the data supplied to the Hermite interpolation problem (3.7) will only be given approximately using a compact  $\varepsilon$ -difference stencil about the vertices. If we consider the chart  $\varphi_{v_i}$  centred at the vertex  $v_i \in \mathcal{S}$ , the metric tensor reduces to the identity and the components of the surface gradient at  $v_i$  are simply given by the partial derivatives of  $\hat{f}$  evaluated at the origin. We approximate the function values and components of the surface gradient supplied in (3.7) by the  $\mathcal{O}(\varepsilon^2)$  stencils

$$\begin{aligned} f(v_i) &\approx \frac{1}{4} (f_{(+,+)} + f_{(+,-)} + f_{(-,+)} + f_{(-,-)}) \\ \mathbf{e}_1(v_i) \cdot \nabla_{\mathcal{S}} f(v_i) &\approx \frac{1}{4\varepsilon} (f_{(+,-)} - f_{(-,-)} + f_{(+,+)} - f_{(-,+)}), \\ \mathbf{e}_2(v_i) \cdot \nabla_{\mathcal{S}} f(v_i) &\approx \frac{1}{4\varepsilon} (f_{(-,+)} - f_{(-,-)} + f_{(+,+)} - f_{(+,-)}) \end{aligned} \quad (3.26)$$

where  $\varepsilon > 0$  is a constant and  $f_{(\pm,\pm)} = f \circ \varphi_{v_i}^{-1}(\pm\varepsilon, \pm\varepsilon)$ . At each time step, the footpoints of the four stencil points are determined by numerical integration backwards in time. The interpolated map from the previous iteration is then evaluated at these foot points. This yields approximate data for (3.7) from which a new interpolant is formed as in (3.1). We retain the local truncation error for (3.7) if we choose  $\varepsilon$  such that the error incurred by (3.26) is an  $\mathcal{O}(h^3)$  approximation of function values and  $\mathcal{O}(h^2)$  approximation of the derivatives. In practice the value of  $\varepsilon$  is fixed beforehand such that the error incurred by (3.26) is negligible compared to the local truncation error due to the interpolation for the discretizations considered.

A similar result regarding the accuracy of a PS interpolant using approximated Hermite data was given in [47] using a different interpolation strategy and data fitting algorithm. We adapt their proof by transforming a spherical spline into a projected PS bivariate spline in local tangent plane coordinates.

**Theorem 1.** *Let  $f \in C^3(\mathcal{S})$  and suppose that  $D^\alpha f(v_i)$  is given approximately to order  $\mathcal{O}(h^{3-|\alpha|})$  for  $|\alpha| \leq 1$ . Let  $s \in S_2^1(\Delta_{PS})$  be the solution to the interpolation problem (3.7) for the approximated data. Then the following holds*

$$\|f - s\|_{C(\mathcal{S})} \leq K \left[ h^3 \|f\|_{C^3(\mathcal{S})} + \max_{v \in \mathcal{V}} (|f(v) - s(v)| + h \|\nabla f(v) - \nabla s(v)\|) \right], \quad (3.27)$$

where  $K$  depends on the smallest angle  $\alpha$  in the triangulation and  $\kappa = \sup_{\xi \in \mathcal{S}} \kappa(\xi)$  where

$$\kappa(\xi) = \max_{v \in \mathcal{V}} \{ \|J_{\xi,v}(v)\|_2, \|J_{v,\xi}(v)\|_2 \}. \quad (3.28)$$

PROOF. Let  $f_i, \sigma_{v_i}$  be the exact function values and directional derivatives at the vertices and let  $\tilde{f}_i, \tilde{\sigma}_i$  be their approximations according to the statement of the theorem. Let  $p \in S_2^1(\Delta_{PS})$  be the interpolatory spline solving (3.7) for the exact function and derivative data at the vertices and let  $\mathbf{v} \in \mathcal{S}$ . Then using (3.9) we have that

$$|f(\mathbf{v}) - s(\mathbf{v})| \leq Ch^3 \|f\|_{C^3(\mathcal{S})} + |p(\mathbf{v}) - s(\mathbf{v})|. \quad (3.29)$$

Suppose that  $\mathbf{v} \in \mathcal{S}$  is contained in the spherical triangle formed by the vertices  $v_1, v_2, v_3$ . The second term in (3.29) can be estimated by interpolating the functions  $\hat{s} = s \circ \varphi_{\mathbf{v}}^{-1}$  and  $\hat{p} = p \circ \varphi_{\mathbf{v}}^{-1}$  in a planar triangle  $\hat{T}$  formed by the vertices  $w_i = \varphi_{\mathbf{v}}^{-1}(v_i)$  in the tangent plane at  $\mathbf{v}$ . Let  $\hat{h}$  the maximum edge length  $\hat{T}$ , which is bounded above by  $h$ . By the stability of the nodal minimal determining set for the space of bivariate splines on the PS split [41] and using (3.25) we get that

$$\begin{aligned} |s(\mathbf{v}) - p(\mathbf{v})| &= |\hat{s}(0,0) - \hat{p}(0,0)| \leq \max_{w_i} \left( |\hat{p}(w_i) - \hat{s}(w_i)| + \hat{h} \|\sigma_{v_i} J_{\mathbf{v},v_i}(w_i) - \tilde{\sigma}_{v_i} J_{\mathbf{v},v_i}(w_i)\| \right) \\ &\leq \max_{v_i} (|p(v_i) - s(v_i)| + h\kappa^2 \|\sigma_{v_i} - \tilde{\sigma}_{v_i}\|) \end{aligned} \quad (3.30)$$

which establishes the claim.  $\square$

### 3.3. Error Estimates

In this section we provide error estimates for the solution of (2.3) and (2.6) using the CM method, yielding a theoretical justification of the results in section 4. We will use the following quantity to measure the error between two continuous maps  $F, G : \mathcal{S} \rightarrow \mathcal{S}$

$$\|F - G\|_{C(\mathcal{S}, \mathcal{S})} := \sup_{x \in \mathcal{S}} d_{\mathcal{S}}(F(x), G(x)) = \sup_{x \in \mathcal{S}} 2 \arcsin(\|F(x) - G(x)\|/2), \quad (3.31)$$

which is the supremum of the arc length distance between  $F(x)$  and  $G(x)$ . Combining the estimates (3.14), (3.19) with (3.27) for each component of  $\mathbf{X}_{[t,0]}$  yields an estimate on the local truncation error due to the spatial discretization of the backward characteristic map. In particular, if the data supplied to (3.7) satisfy the conditions of theorem (1) and (3.18) holds, then for a fixed  $t$  there exists a  $C > 0$  such that

$$\|\mathcal{J}_h[\mathbf{X}_{[t,0]}] - \mathbf{X}_{[t,0]}\|_{C(\mathcal{S}, \mathcal{S})} \leq Ch^3. \quad (3.32)$$

**Lemma 2.** *Suppose that  $T \in C^1(\mathcal{S}, \mathcal{S})$  satisfies  $\|T - id_{\mathcal{S}}\|_{C(\mathcal{S}, \mathcal{S})} = \mathcal{O}(\Delta t)$ , then for all  $f : \mathcal{S} \rightarrow \mathbb{R}$  sufficiently differentiable the following holds:*

$$\|\mathcal{I}_h[f \circ T] - \mathcal{I}_h[f] \circ T\|_{C(\mathcal{S}, \mathcal{S})} = \mathcal{O}(\Delta t h^2). \quad (3.33)$$

PROOF. Using (3.9) an analogous estimate was given in [53] (Lemma 3.1).

**Theorem 3.** *Using an  $s$ -stage RK integration scheme and quadratic spherical spline interpolant, the approximation  $\mathcal{X}_{[T,0]}(\mathbf{x})$  is consistent with  $\mathbf{X}_{[T,0]}(\mathbf{x})$  to order*

$$\|\mathbf{X}_{[T,0]} - \mathcal{X}_{[T,0]}\|_{C(\mathcal{S}, \mathcal{S})} = \mathcal{O}(T \min(h^2, h^3 \Delta t^{-1}) + T \Delta t^s). \quad (3.34)$$

PROOF. Suppose initially that  $\mathcal{X}_{[t_{n-1},0]} = \mathbf{X}_{[t_{n-1},0]}$ . The inverse of the submap  $\mathcal{X}_{[t_n, t_{n-1}]}$  computed using an  $s$ -stage RK integration scheme forwards in time is an  $\mathcal{O}(\Delta t^{s+1})$  approximation to the inverse of  $\mathbf{X}_{[t_n, t_{n-1}]}$  as measured using (3.31). Letting  $\mathcal{E}_{[t_n, t_{n-1}]} = \mathbf{X}_{[t_n, t_{n-1}]} \circ \mathcal{X}_{[t_n, t_{n-1}]}^{-1}$  we split the error incurred by (3.1) as follows

$$\begin{aligned} \|\mathcal{X}_{[t_n,0]} - \mathbf{X}_{[t_n,0]}\|_{C(\mathcal{S}, \mathcal{S})} &\leq \|\mathbf{X}_{[t_{n-1},0]} \circ \mathcal{X}_{[t_n, t_{n-1}]} - \mathbf{X}_{[t_n,0]}(\mathbf{x})\|_{C(\mathcal{S}, \mathcal{S})} \\ &\quad + \|\mathcal{J}_h[\mathbf{X}_{[t_{n-1},0]} \circ \mathcal{X}_{[t_n, t_{n-1}]}] - \mathbf{X}_{[t_{n-1},0]} \circ \mathcal{X}_{[t_n, t_{n-1}]} \|_{C(\mathcal{S}, \mathcal{S})} \\ &:= E_{\Delta t} + E_{h, \Delta t}. \end{aligned} \quad (3.35)$$

Using the Lipschitz continuity of  $\mathbf{X}_{[t_{n-1},0]}$  we can estimate the first term as

$$\begin{aligned} E_{\Delta t} &= \|(\mathbf{X}_{[t_{n-1},0]} - \mathbf{X}_{[t_{n-1},0]} \circ \mathcal{E}_{[t_{n-1}, t_n]}) \circ \mathcal{X}_{[t_n, t_{n-1}]}\|_{C(\mathcal{S}, \mathcal{S})} \\ &\leq \|\mathbf{X}_{[t_{n-1},0]} - \mathbf{X}_{[t_{n-1},0]} \circ \mathcal{E}_{[t_{n-1}, t_n]}\|_{C(\mathcal{S}, \mathcal{S})} \\ &\leq C \|\text{id}_{\mathcal{S}} - \mathcal{E}_{[t_{n-1}, t_n]}\|_{C(\mathcal{S}, \mathcal{S})} = \mathcal{O}(\Delta t^{s+1}), \end{aligned} \quad (3.36)$$

where  $C$  is the Lipschitz constant of  $\mathbf{X}_{[t_{n-1},0]}$ . The second term in (3.35) can be estimated by applying (3.32) and (3.33), yielding

$$\begin{aligned} E_{h, \Delta t} &\leq \|\mathcal{J}_h[\mathbf{X}_{[t_{n-1},0]} \circ \mathcal{X}_{[t_n, t_{n-1}]}] - \mathcal{J}_h[\mathbf{X}_{[t_{n-1},0]}] \circ \mathcal{X}_{[t_n, t_{n-1}]}\|_{C(\mathcal{S}, \mathcal{S})} \\ &\quad + \|(\mathcal{J}_h[\mathbf{X}_{[t_{n-1},0]}] - \mathbf{X}_{[t_{n-1},0]}) \circ \mathcal{X}_{[t_n, t_{n-1}]}\|_{C(\mathcal{S}, \mathcal{S})} \\ &= \mathcal{O}(\Delta t h^2 + h^3). \end{aligned} \quad (3.37)$$

The global truncation error for  $N_t = T \Delta t^{-1}$  steps is then given by (3.34), establishing the claim.  $\square$

The order of convergence of the approximation of (2.10) using  $\mathcal{X}_{[t,0]}$  will in general be dictated by the modulus of continuity of  $\phi_0$  when measured in the sup-norm. It follows that for any Lipschitz continuous initial condition  $\phi_0$  the order of convergence of the solution will be equivalent to the order given by (3.34). In the weaker case that  $\phi_0$  is only of bounded variation, then the convergence of the approximated solution will be of the same order as (3.34) in the  $L^1(\mathcal{S})$  norm. This follows from the fact that functions of bounded variation are almost everywhere differentiable and hence Lipschitz continuous up to a set of measure zero.

The solution to (2.6a) given by (2.9) for  $\rho_0 = 1$  is approximated as

$$\rho(\mathbf{x}, t) = J_\mu(\mathcal{X}_{[t,0]}). \quad (3.38)$$

The computation of (3.38) is performed using the matrix representation of the differential of the map expressed in local tangent plane coordinates. In the orthonormal bases  $\{\gamma_{\mathbf{x}}^{(1)}, \gamma_{\mathbf{x}}^{(2)}\}$  and  $\{\gamma_{\boldsymbol{\xi}}^{(1)}, \gamma_{\boldsymbol{\xi}}^{(2)}\}$  for  $T_{\mathbf{x}}\mathcal{S}$  and  $T_{\boldsymbol{\xi}}\mathcal{S}$  respectively, the matrix representation of the linear map  $d\mathcal{X}_{[t,0]}$  is given by

$$[d\mathcal{X}_{[t,0]}]_{i,j} = \langle \gamma_{\boldsymbol{\xi}}^j, \nabla \mathcal{X}_{[t,0]} \cdot \gamma_{\mathbf{x}}^i \rangle \quad (3.39)$$

where  $\nabla \mathcal{X}_{[t,0]}$  is the Euclidean gradient of the map computed using (3.15). If we assume that the error in the differential of the map is small, then the sup-norm error of the approximated density satisfies

$$\begin{aligned} \|J_\mu(\mathcal{X}_{[t,0]}) - J_\mu(\mathbf{X}_{[t,0]})\|_{L^\infty(\mathcal{S})} &\approx \|\text{tr}((d\mathbf{X}_{[t,0]})^{-1}(d\mathcal{X}_{[t,0]} - d\mathbf{X}_{[t,0]}))\|_{L^\infty(\mathcal{S})} \\ &= \mathcal{O}(\|d\mathcal{X}_{[t,0]} - d\mathbf{X}_{[t,0]}\|_{L^\infty(\mathcal{S})}). \end{aligned} \quad (3.40)$$

## 4. Numerical Tests

In this section we present numerical tests of the CM method for the solution of (2.6) and (2.3). We begin with a numerical verification of the method and our implementation using a standard test case suite as outlined in [37, 54]. The tests performed affirm the theoretically expected rate of convergence for the characteristic map (3.34) along with the tracer and density errors in each case. Additionally, we demonstrate how the method exactly preserves correlations between multiple advected quantities. Thereafter, we emphasize some unique advantages of determining the evolution of  $\phi$  via (2.10). In particular, we showcase how the method possesses arbitrary resolution with a zoom-in on the solution for an initial condition containing arbitrary scales in a complex flow environment.

### 4.1. Numerical verification

In this section we present a numerical verification of the CM method and our implementation using convergence tests based on a standard suite of velocity fields [54, 37]. The tests are organized into solid body rotation 4.1.3, deformational 4.1.4, and compressible 4.1.5 velocity fields. In supplement to these tests we demonstrate how the CM method exactly preserves non-linear correlations between multiple advected quantities.

#### 4.1.1. Implementation details

The numerical tests were all implemented in Python and run on a Linux workstation with an Intel core i5-8250U (8 logical processors) with 16 GB of RAM. The spherical triangulation is constructed using the Python package Stripy [55] which provides a wrapper to the package STRIPACK [56]. The point in triangle querying was performed using the Python binding supported by the package Libigl [57]. The tests are all performed on successive uniform refinements of an icosahedral discretization of the sphere [58] (see table 1). We note however that the formulation and implementation are essentially agnostic to the particular spherical triangulation. Based on the convergence rate (3.34), we demonstrate the global second-order accuracy of the method by refining  $T/N_t = \Delta t$  proportionally to  $h$ . In particular, we consider  $N_t = 2^k + 10$  where  $k$  is the number of refinements of the icosahedral discretization. A value of  $\varepsilon = 10^{-5}$  is chosen for the  $\varepsilon$ -difference stencils (3.26) in each test which effectively limits the machine precision to approximately  $10^{-12}$ .

$k$	0	1	2	3	4	5	6	7	8
$N_v$	12	42	162	642	2562	10242	40062	163842	655362
$N_\Delta$	20	80	320	1280	5120	20480	81920	327680	1310720
$h$	1.10715	0.62832	0.32637	0.16483	0.08263	0.04134	0.02067	0.01034	0.00517

Table 1: Number of vertices ( $N_v$ ), simplices ( $N_\Delta$ ), and maximum edge length  $h$  for the  $k^{\text{th}}$  refinement of the icosahedral discretization of the sphere.

#### 4.1.2. Initial conditions and error norms

The forthcoming numerical tests, with the exception of the moving vortices test, are designed such that the initial condition returns to itself at the final integration time. Consequently, the backward characteristic map at time  $T$  is given by the identity map on the sphere. We assess the accuracy of the method using an approximation of the following quantities

$$\text{tracer } (l^\infty) \text{ error} = \frac{\|\mathcal{X}_{[T,0]}^* \phi_0 - \phi(\cdot, T)\|_{L^\infty(\mathcal{S})}}{\|\phi(\cdot, T)\|_{L^\infty(\mathcal{S})}}, \quad (4.1a)$$

$$\text{tracer } (l^1) \text{ error} = \frac{\|\mathcal{X}_{[T,0]}^* \phi_0 - \phi(\cdot, T)\|_{L^1(\mathcal{S})}}{\|\phi(\cdot, T)\|_{L^1(\mathcal{S})}}, \quad (4.1b)$$

$$\text{map-(i) error} = \|\mathcal{X}_{[T,0]}^{(i)} - \text{id}_S^{(i)}\|_{L^\infty(\mathcal{S})}, \quad (4.1c)$$

$$\text{density error} = \|1 - J_\mu(\mathcal{X}_{[T,0]})\|_{L^\infty(\mathcal{S})} \quad (4.1d)$$

where  $\text{id}_S^{(i)}$  is the  $i$ -th component of the identity map and  $\phi(\cdot, T)$  is the expected solution at the final integration time. The sup-norm is approximated as the maximum value over  $10^6$  points sampled from a random uniform distribution over the domain and the  $L^1$  norm is approximated using the average over the vertices in the triangulation as

$$\|f\|_{L^1(\mathcal{S})} \approx \sum_{T \in \Delta} \sum_{v_i \in T} f(v_i) |T|/3. \quad (4.2)$$

We note that it is common to assess the accuracy of a numerical method for linear advection using discrete analogues of (4.1) in the  $\ell^\infty$  and  $\ell^2$  norms. We have chosen a finer approximation of the continuous error measures (4.1) here in an effort to more closely support the estimates given in section 3.3 and to emphasize the functional definition of the backward characteristic map.

For expressions involving spherical coordinates, we use the convention that the spherical coordinate transform is defined by

$$\eta : [0, 2\pi) \times (0, \pi) \cup \{(\pi, 0), (\pi, \pi)\} \rightarrow \mathcal{S} \subset \mathbb{R}^3, \quad (\lambda, \theta) \mapsto (\sin \theta \cos \lambda, \sin \theta \sin \lambda, \cos \theta). \quad (4.3)$$

We consider three different initial conditions; the first of which consists of two symmetrically located cosine-bells

$$g_i(\lambda, \theta) = \begin{cases} \frac{1}{2} [1 + \cos(\pi r_i/r)] & \text{if } r_i < r, \\ 0 & \text{otherwise,} \end{cases} \quad (4.4)$$

where  $r = 1/2$  is taken to be the base radius of each cosine bell and  $r_i = r_i(\lambda, \theta)$  is the great-circle distance from the centre of the bell located at  $(\lambda_i, \theta_i)$ , given by

$$r_i(\lambda, \theta) = \arccos(\sin \theta_i \sin \theta + \cos \theta_i \cos \theta \cos(\lambda - \lambda_i)). \quad (4.5)$$

The initial condition is then defined as

$$\phi(R, \theta) = b + g_1(R, \theta) + g_2(R, \theta), \quad (4.6)$$

where  $b = 0.1$  and the centres of each bell are chosen to be  $(\lambda_1, \theta_1) = (\pi/6, 0)$  and  $(\lambda_2, \theta_2) = (-\pi/6, 0)$ . The second initial condition, designed to assess the shape-preserving properties of the method, consists of two Zalesak disks [59] defined by

$$\phi(\lambda, \theta) = \begin{cases} 1 & \text{if } r_i \leq r \text{ and } |\lambda - \lambda_i| \geq r/6 \text{ for } i = 1, 2, \\ 1 & \text{if } r_i \leq r \text{ and } |\lambda - \lambda_1| < r/6 \text{ and } \theta - \theta_1 < -\frac{5}{12}r, \\ 1 & \text{if } r_i \leq r \text{ and } |\lambda - \lambda_2| < r/6 \text{ and } \theta - \theta_2 > \frac{5}{12}r, \\ 0.1 & \text{otherwise.} \end{cases} \quad (4.7)$$

The third initial condition we consider is a sum of spherical harmonics of all degrees  $(\ell, m)$  up to  $\ell = 32$  which are multiplied by a randomly generated real coefficient sampled from a uniform distribution from  $-1$  to  $1$ . We consider this last initial condition since it is highly irregular and does not have compact support as the initial conditions (4.6) and (4.7) do. Based on the regularity properties of these initial conditions and the estimates provided in section 3.3, the accuracy of the solutions for the cosine-bell (CB) and random spherical harmonics (rSph) are assessed using (4.1a) whereas the solution for the slotted cylinder (SC) is assessed using (4.1b). We note that in every test performed, the approximation of  $\mathcal{X}_{[T,0]}$  was accurate enough at the grid points such that the error (4.1b) computed for the Zalesak disks was identically zero at every refinement except for  $k = 0, 1$ , we have thus not included these results in the forthcoming convergence plots.

In an effort to demonstrate the geometric flexibility of the method, the tests are performed on a sphere rotating about various axes. The inertial and rotating frames of reference are transformed between one another via a rotation matrix  $R(t) \in \text{SO}(3)$  parameterizing the rigid body rotation. Let  $\mathbf{x} = (x, y, z)$  be standard Cartesian coordinates, with corresponding basis vector fields  $\mathbf{e}_1, \mathbf{e}_2, \mathbf{e}_3$ . A basis of vector fields in the rotating system is given by  $\mathbf{e}'_i = R(t)\mathbf{e}_i$ . Let  $\varphi : \mathbb{R}^3 \rightarrow \mathbb{R}^3, \mathbf{x} \mapsto R(t)\mathbf{x}$  also denote the coordinate transformation from the inertial to the co-rotating system. If the velocity field has components  $(\tilde{u}^1, \tilde{u}^2, \tilde{u}^3)$  in the rotating frame then we can express the velocity field in the inertial frame as

$$\mathbf{u} = \sum_{i=1}^3 (\tilde{u}^i \circ \varphi)(\mathbf{x}) R^T(t) \mathbf{e}'_i. \quad (4.8)$$

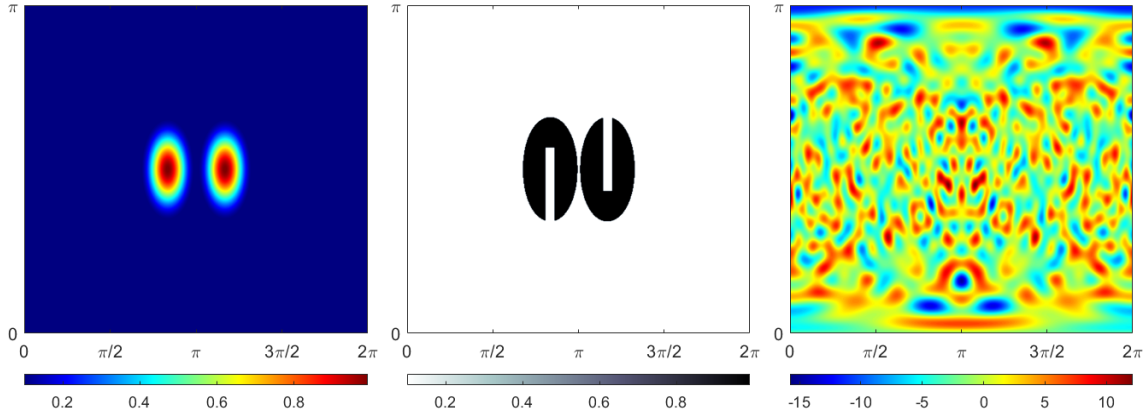


Figure 2: Cosine bell (4.6) (left), two Zalesak disks (4.7) (middle), and random spherical harmonics initial conditions.

#### 4.1.3. Test case 1: Solid body rotation

The first test case considered is the solid body rotation for a rotation axis controlled by an angle of inclination  $\alpha$  from the point  $(0, 0, 1)$  along the direction of the positive  $x$ -axis. The velocity field is given by

$$\mathbf{u}_{sbr} = \mathbf{x} \times d\mathcal{P}_{\mathbf{x}} \nabla \psi, \quad \psi(x, y, z) = \frac{2\pi}{T} (\cos \alpha z - \sin \alpha x), \quad (4.9)$$

restricted to the sphere. The results of the test for values of  $\alpha \in \{0, \pi/2, \pi/4, 1.05\}$  are shown in figure 3. We observe the order of convergence to be slightly greater than the expected second order convergence for each test case.

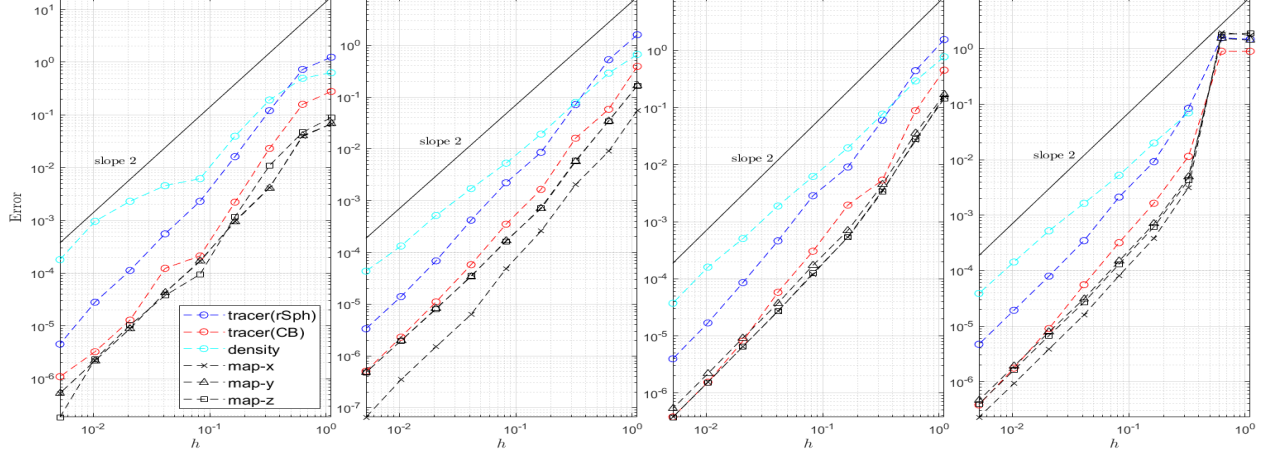


Figure 3: Results for test case 4.1.3 for axes of rotation defined by  $\alpha = 0, \pi/2, \pi/4, 1.05$  from left to right. The final integration time was taken to be  $T = 1$ .

#### 4.1.4. Test case 2: Deformational flows

In this test case we consider five different deformational velocity fields. The first three velocity fields are the reversing deformational test combined with a solid body rotation about the axes defined by  $\alpha = 0, 1.05, \pi/4$  [37]. The transformation into the co-rotating frame  $\varphi_{\beta, \alpha} : \mathbb{R}^3 \rightarrow \mathbb{R}^3$  is formed by rotating about the  $y$ -axis by  $\alpha$  followed by a rotation about the  $z'$ -axis by angle  $\beta(t) = 2\pi t/T$ . The velocity field is given by

$$\begin{aligned} \mathbf{u}(\mathbf{x}, t) &= \mathbf{u}_{sbr}(\mathbf{x}) + \mathbf{u}_d(\mathbf{x}, t), \\ \mathbf{u}_d(\mathbf{x}', t) &= \mathbf{x}' \times d\mathcal{P}_{\mathbf{x}'} \nabla \psi_r(\mathbf{x}', t), \\ \psi_r(\mathbf{x}', t) &= 2y'^2 \cos(\pi t/T), \end{aligned} \quad (4.10)$$

restricted to the sphere. The gradient of the stream function is computed with respect to the primed coordinates and  $\mathbf{u}(\mathbf{x}, t)$  is evaluated in the inertial frame of reference using (4.8).

The fourth and fifth velocity fields considered are the static and moving vortices velocity [54]. The test consists of two circular vortices with antipodal centres positioned at the equator which we consider as rotating about the  $z$ -axis in the moving case. Let  $(\lambda', \theta')$  be spherical coordinates resulting from the transformation  $\eta^{-1} \circ \varphi_{\pi/2}(\mathbf{x})$  where  $\varphi_{\pi/2}$  is a rotation about the  $x$ -axis by angle  $\pi/2$ . The radial distance from the centre of the vortex is  $\rho = \rho_0 \sin(\theta')$  and the angular velocity in dimensionless units is given by

$$\omega(\theta') = \begin{cases} \frac{2\pi}{T} \frac{3\sqrt{3}}{2\rho} \text{sech}^2(\rho) \tanh(\rho) & \text{if } \rho \neq 0, \\ 0 & \text{if } \rho = 0. \end{cases} \quad (4.11)$$

In the rotating frame of reference, we have that  $\dot{\lambda}' = \omega(\theta') \csc(\theta')$ ,  $\dot{\theta}' = 0$  and the velocity field in the inertial frame of reference is given by

$$\begin{aligned} \mathbf{u}(\mathbf{x}) &= \mathbf{u}_s(\mathbf{x}) + \mathbf{u}_v(\mathbf{x}), \\ \mathbf{u}_v(\mathbf{x}') &= -y'\omega(\theta')\mathbf{e}'_1 + x'\omega(\theta')\mathbf{e}'_2, \end{aligned} \quad (4.12)$$

where  $\mathbf{u}_s$  is given by (4.9) for  $\alpha = 0$  and the velocity field  $\mathbf{u}_v$  is evaluated in the inertial frame using (4.8) where  $\varphi$  is a rotation about the  $z$ -axis by angle  $\beta(t) = 2\pi t/T$ . The solution to the advection equation for the velocity field (4.12) is given by

$$\phi(\lambda', \theta', t) = 1 - \tanh \left[ \frac{\rho}{5} \sin(\lambda' - \omega(\theta')t) \right], \quad (4.13)$$

where the coefficients  $1/5$  along with  $\rho_0 = 3$  are chosen so that the deformation in the flow is smooth [60, 61]. We test using both the rotating and static form of the vortex flow.

The results of the numerical test are shown in figure 5. The tests are performed with final integration times of  $T = 1, 5$  for the velocity fields defined by (4.10) and  $T = 1, 2$  for the vortices flow (4.12). Increasing the final integration increases the error by approximately one order of magnitude, which is consistent with the error estimates and is attributed to the larger  $T$  and  $\Delta t$ . The effect of the axis of rotation is insignificant for the velocity fields defined by (4.10) and we observe the theoretically expected second-order convergence. The effect of rotation is negligible for (4.12) and we observe the expected global second-order convergence, although this test required more refinements before reaching the asymptotic regime.

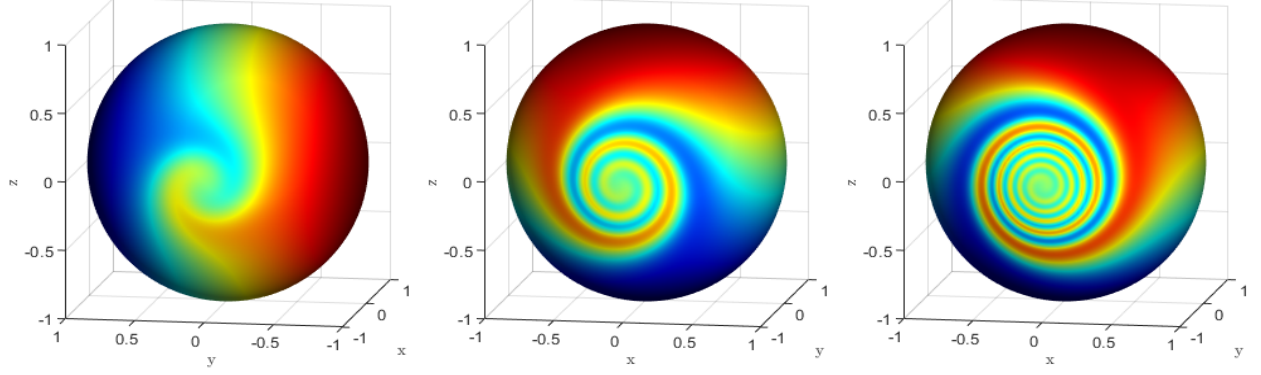


Figure 4: Numerical solution for test case 2 at times  $t = 0.5, 1, 2$  from left to right respectively.

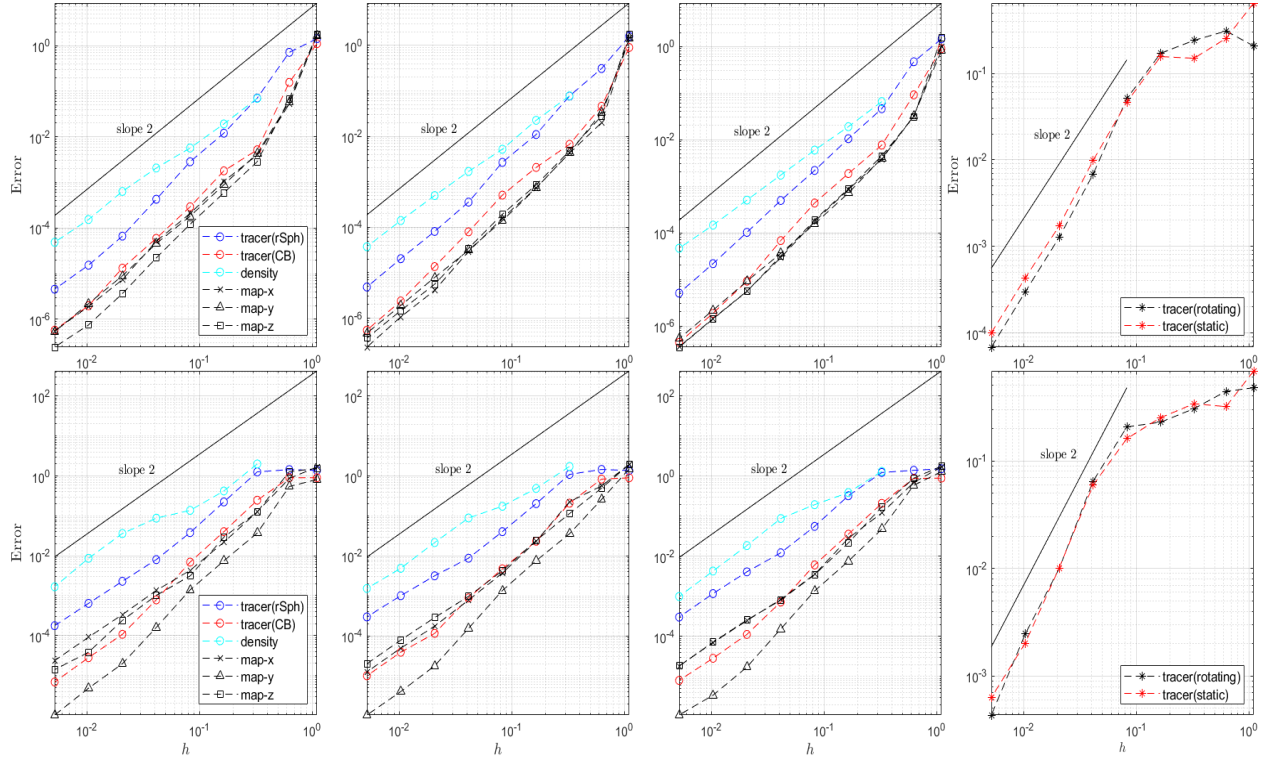


Figure 5: Results for test case 4.1.4, first three columns from left to right correspond to the velocity field (4.10) with background rotations defined by  $\alpha = 0, \pi/4, 1.05$  respectively. The final integration times were taken to be  $T = 1$  (top row) and  $T = 5$  (bottom row). The right most column corresponds to the velocity field (4.12) with and without rotation for final integration times  $T = 1$  (top) and  $T = 2$  (bottom).



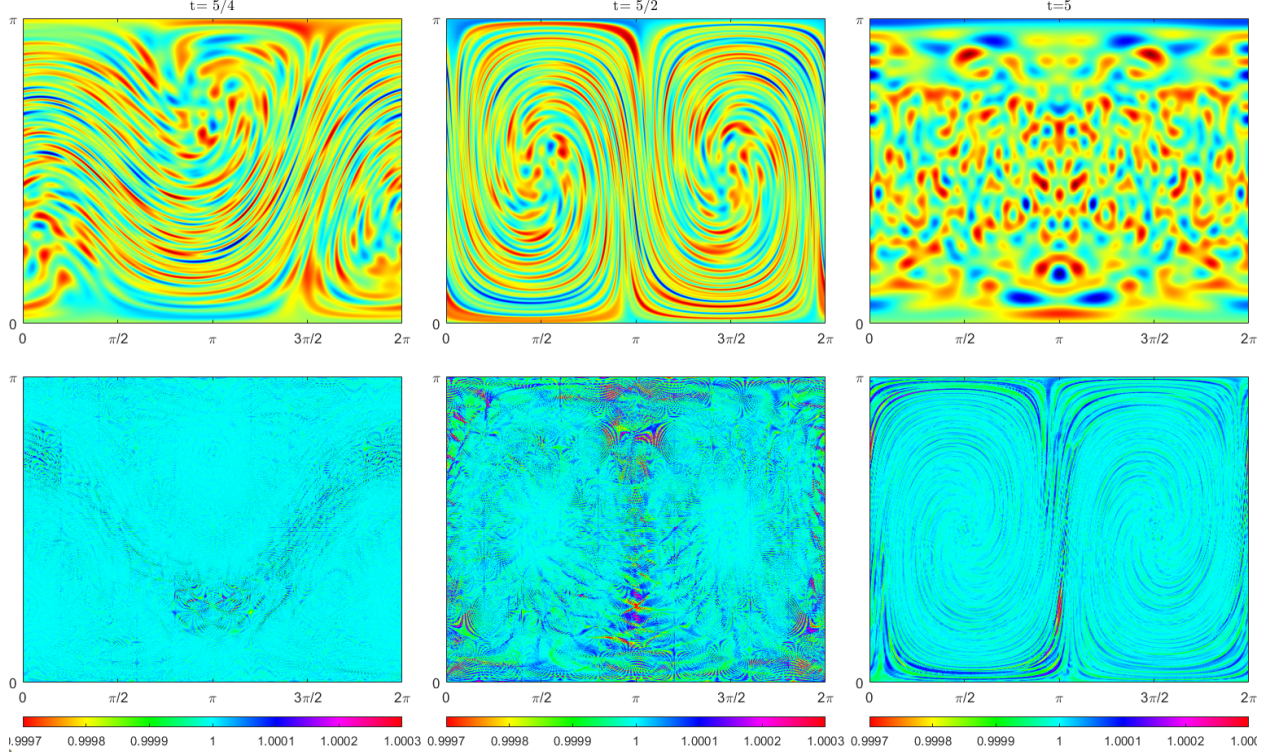


Figure 6: Numerical solution at  $t = 1.25, 2.5, 5$  (left-right) for the random spherical harmonics tracer (top row) and the density (bottom row) with transporting velocity (4.10) with  $\alpha = \pi/4$  and  $T = 5$ .

#### 4.1.5. Test case 3: Compressible velocity field

In this test we consider a velocity field with non-zero divergence. Expressed in spherical coordinates, the velocity field is given by [37]

$$\begin{aligned} u(\lambda, \theta, t) &= -\sin^2(\lambda/2) \sin(2\theta) \sin^2(\theta) \cos(\pi t/T), \\ v(\lambda, \theta, t) &= \frac{1}{2} \sin(\lambda) \sin^3(\theta) \cos(\pi t/T), \end{aligned} \quad (4.14)$$

which is expressed in Cartesian coordinates using (4.3) and the fact that  $(u, v) = (\dot{\lambda}(t) \csc(\theta(t)), \dot{\theta}(t))$ . The test is designed to return to itself at the final integration time.

The compressibility of the velocity field manifests itself as a change in density of the fluid throughout the evolution. The numerical solution for the tracer and tracer density shown in figure 8 illustrates this property. Since the action of the solution operator defined by (2.9) and (2.10) are independent of the compressibility of the velocity field, the formulation needs no modification. The results of the convergence test are shown in figure 7, affirming the theoretically predicted rate of convergence.

#### 4.1.6. Test case 4: Correlated tracer transport

It is desirable for transport schemes to preserve certain functional relations in the advected quantities. We evaluate the distortion of these relations due to the error introduced during computation using the diagnostic test case 3 provided in [62]. As initial condition we consider two non-linearly correlated quantities,  $q_1$  and  $q_2$ , defined by

$$\begin{aligned} q_1(\lambda, \theta) &= \begin{cases} 0.1 + 0.45 [1 + \cos(\pi r_1/r)] & \text{if } r_1 < r, \\ 0.1 + 0.45 [1 + \cos(\pi r_2/r)] & \text{if } r_2 < r, \\ 0.1 & \text{otherwise,} \end{cases} \\ q_2(\lambda, \theta) &= -0.8q_1^2(\lambda, \theta) + 0.9. \end{aligned} \quad (4.15)$$



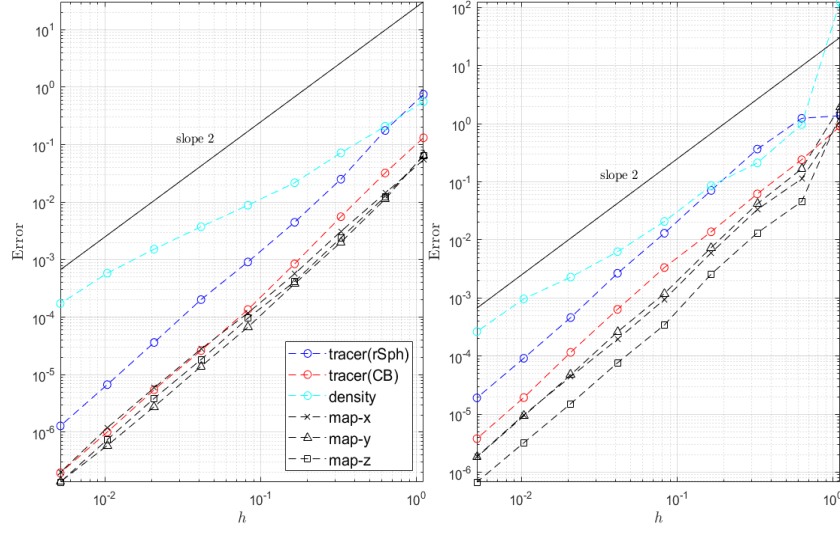


Figure 7: Results for test case 4.1.5 with final integration times  $T = 1$  (left) and  $T = 5$  (right).

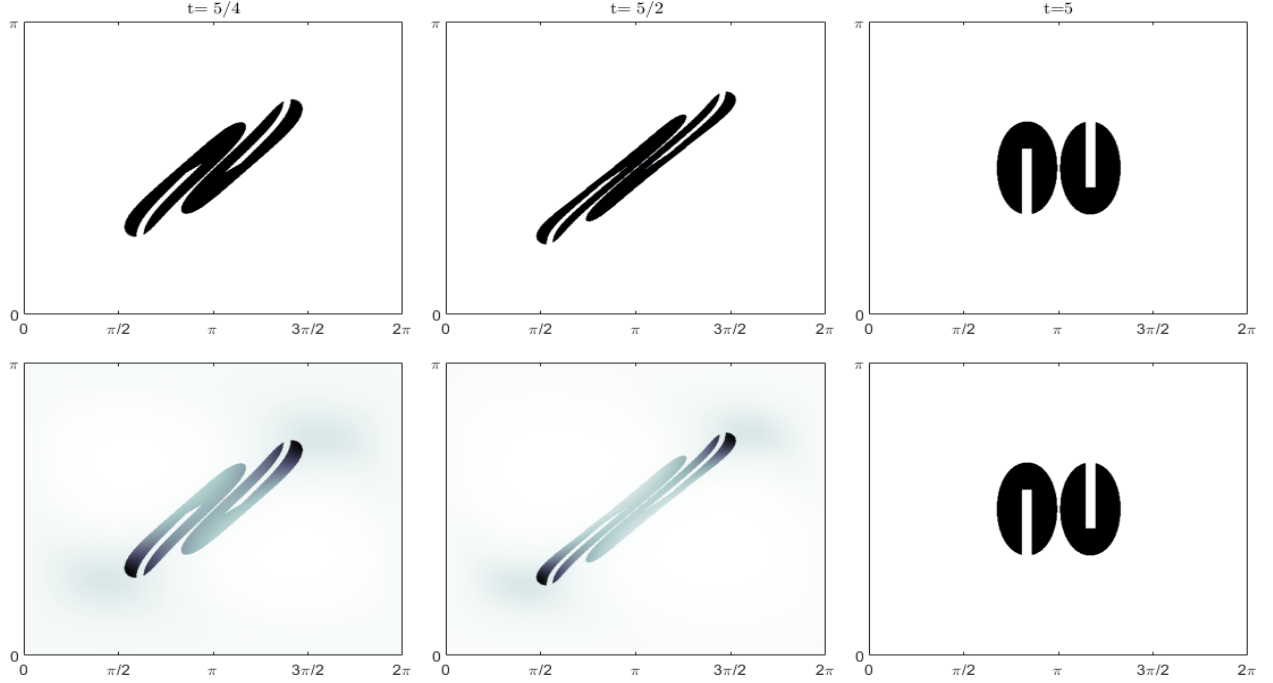


Figure 8: Numerical solution for test case 4.1.5 with final integration time  $T = 5$  with initial condition (4.7). Transported tracer  $\phi_0 \circ \mathcal{X}_{[t,0]}$  (top row) and tracer density  $\phi_0 \circ \mathcal{X}_{[t,0]} \cdot J_\mu(\mathcal{X}_{[t,0]})$  (bottom row) at times  $t = 5/4, 5/2, 5$  from left to right.

As transporting velocity field, we use (4.10) with  $\alpha = 1.05$  and final integration time  $T = 5$ . The functional relation between these initial conditions is assessed using a scatter plot of  $q_2$  plotted against  $q_1$  at time  $t = T/2$  when the deformation is the greatest. Each advected quantity is sampled at  $200^2$  evenly spaced points in the computational domain for three different grid spacings. The results of the numerical test are presented in figure 9. As a consequence of the problem formulation using the CM method and the analytic definition of the initial conditions, the functional relation between the tracers is preserved *exactly*. Sampling each advected quantity at time  $t = T/2$  via (2.10) requires a single evaluation of  $\mathcal{X}_{[T/2,0]}$ . As a

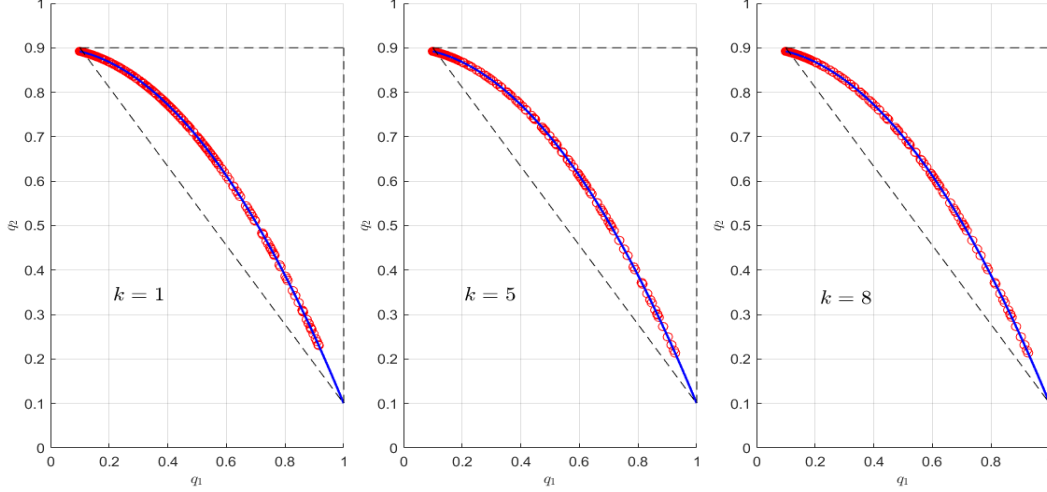


Figure 9: Numerical mixing test for non-linearly correlated cosine-bell initial conditions (4.15) at refinements  $k = 1, 5, 8$  (left to right),  $q_2 \circ \mathcal{X}_{[T/2, 0]}$  plotted against  $q_1 \circ \mathcal{X}_{[T/2, 0]}$ , with grid spacings indicated. The transporting velocity field was (4.10), final integration time  $T = 5$ , initial conditions sampled at  $t = 5/2$ . The exact relation is indicated by the blue line and the computed results are plotted in red.

result, the tracers are evaluated at the same location, thus exactly maintaining their correlations over time.

We emphasize that the error incurred by the transported tracers is *advective* in nature, resulting from an approximation of the location of evaluation. In this formulation, the effects of numerical mixing are not present since a single evaluation of the approximated backward characteristic map is used to advect each tracer. This property is not limited to two tracers and these results can be extended to arbitrarily many tracers with varying correlations while only incurring the added computational cost of the evaluation (2.10).

## 4.2. Numerical Experiments

In this section we present some numerical experiments designed to highlight some unique features of the method. First, we present a remapping technique which can be used to improve the accuracy of a simulation by resolving larger deformations generated by the velocity field. Thereafter we showcase the capacity of the method to advect arbitrarily defined quantities via the transport of the Mandelbrot set on the sphere under the velocity field (4.10) with  $\alpha = 1.05$  and a final integration time of  $T = 5$ .

### 4.2.1. Submap Decomposition

In this section we give a description of the technique of submap decomposition to improve the accuracy of the method. The technique of submap decomposition has been successfully applied to resolve fast-growing gradients of the vorticity for the incompressible Euler equations [35]. Here, we consider a similar strategy to the submap decomposition outlined in [35] and compare the benefits in terms of accuracy improvements for the solutions to (2.6) for some non-adaptive remapping strategies.

The remapping strategy exploits the fact that the initial condition of (2.3) is given by the identity map. Since the identity map need not be interpolated, the footpoint computations on the first iteration incur no error due to spatial discretization. This property can be utilized along with the semi-group structure of the map to garner better accuracy in the solution. At time steps  $\tau_i \in \{t_0, t_1, \dots, t_n\}$  where  $0 < i \leq n - 1$  we store the map  $\mathcal{X}_{[\tau_i, 0]}$  in memory and reinitialize  $\mathcal{X}_{[\tau_i, \tau_i]} = \text{id}_S$ . A submap is then computed over the interval  $[\tau_i, \tau_{i+1}]$  using (3.1) on the time steps  $t_j$  such that  $\tau_i \leq t_j < \tau_{i+1}$ . If the remapping is performed  $m$  times then the numerical approximation of the backward characteristic map at  $t_n$  is computed using the semi-group property as

$$\mathcal{X}_{[t_n, 0]} = \mathcal{X}_{[\tau_1, 0]} \circ \mathcal{X}_{[\tau_2, \tau_1]} \circ \dots \circ \mathcal{X}_{[t_n, \tau_m]}. \quad (4.16)$$

Since the submaps forming the decomposition (4.16) are all initialized as the identity map, at each remapping step we effectively reset the local truncation error due to spatial discretization accumulated over the previous

Rotating Vortices ( $T = 2$ )			
$k$	every 10 steps	every 25 steps	No remap
4	1.6908e-02	7.3803e-02	1.8087e-01
5	2.9750e-03	1.2338e-02	1.1582e-01
6	2.0803e-04	8.7780e-04	3.2575e-02
7	2.8745e-05	8.6162e-05	4.3428e-03
8	2.5355e-06	1.0978e-05	5.8284e-04
Deformational ( $\alpha = 1.05, T = 5$ )			
4	8.1324e-02	9.0085e-02	8.9054e-01
5	1.0159e-02	1.1500e-02	1.2414e-01
6	1.4083e-03	1.5467e-03	1.8207e-02
7	1.8440e-04	2.0179e-04	2.3601e-03
8	2.1918e-05	2.4707e-05	2.7423e-04
Compressible ( $T = 5$ )			
4	8.7950e-03	8.4461e-03	1.9218e-02
5	1.2195e-03	1.5149e-03	3.4576e-03
6	2.1277e-04	2.4879e-04	5.9590e-04
7	3.6290e-05	4.2100e-05	1.1453e-04
8	5.0425e-06	5.7119e-06	1.9299e-05

Table 2: The error (4.1a) for the random spherical harmonic tracer at different refinement levels and remapping strategies. We have considered the test cases defined by the velocity fields (4.12) for  $T = 2$ , (4.10) for  $\alpha = 1.05$  and  $T = 5$ , along with (4.14) for  $T = 5$ .

iterations. The computation of the backward characteristic map using (4.16) thus improves the accuracy of the method at the expense of increased memory allocation.

**Remark 3.** The remapping steps can be statically enforced or adaptively determined throughout the computation. The adaptive strategy employed in [35] for incompressible flows utilized the error in the Jacobian determinant of the map for some prescribed tolerance. A more ubiquitous adaptive strategy, independent of the compressibility of the velocity field, could be designed based on the conservation laws (2.7). Although, this would require an additional numerical quadrature scheme, introducing a possibly costly computation at each iteration. A low-cost alternative adaptive remapping strategy is to integrate a set of Lagrangian particles forwards in time using a high-order integration scheme. A remapping step can be then be initialized using a prescribed tolerance on the error between the backward characteristic map evaluated at the location of these passive particles and the identity map. We refer to [34] for further details on this strategy. In general, the most effective adaptive remapping strategies will be problem specific, depending on the particular properties of the advected quantity and transporting velocity field.

We present a fixed remapping technique and compare the accuracy gained by increasing the amount of remapping steps. In particular, we compare the error (4.1a) for the test cases defined by the velocity fields (4.12) for  $T = 2$ , (4.10) for  $\alpha = 1.05$  and  $T = 5$ , along with (4.14) for  $T = 5$ . The simulations were run using  $N_t = 250$  time steps for remapping every 10, 25 steps. The results of the test are given in table (4.2.1) where we have included the case without remapping for comparison. The accuracy is shown to improve as the number of remapping steps increases with the greatest improvements observed for the rotating vortices test case.

#### 4.2.2. Arbitrary Set Advection and Subgrid Resolution

We illustrate the capacity of the method to advect functions with poor regularity and represent arbitrarily-fine features by considering the advection of the Mandelbrot set on the sphere. The set is generated via stereographic projection with a cap of arclength  $10^{-9}$  at the north pole. The origin of the stereographic plane (i.e. the south pole) is placed at the point  $-0.235125 + 0.827215i$  in the complex plane defining the Mandelbrot set. The axes are then scaled by a factor of  $4 \times 10^{-5}$ . The velocity field is taken to be (4.10)

with  $\alpha = \pi/4$  and  $T = 5$  and we advect the set using the backward characteristic map  $k = 8$  refinement in the convergence test presented in figure 5. We demonstrate a gradual zoom to a frame size of  $10^{-6}$  in figure 10 for the solution at times  $t = 0$  and  $t = 5$ . This final frame size is chosen based on the results of figure 5, where we expect to observe a discrepancy between the initial condition and solution at the final time for a window width on the same order of magnitude as the  $L^\infty$  error of the backward characteristic map. This serves to demonstrate how every scale in the initial condition is preserved throughout its evolution. We note that since the initial condition is given analytically, the window size is not restricted and could be decreased arbitrarily beyond what is depicted.

## 5. Conclusion

The CM method for the numerical solution of the tracer transport equations on the sphere has been presented. The method employs a novel extrinsic approach to the spatial discretization of the backward characteristic map using a projection-based interpolation framework for manifold-valued data. The resulting globally defined approximation acts via pullback as a solution operator to the tracer transport equations on the sphere. Moreover, the method is formulated to be independent of the compressibility of the transporting velocity field. The error estimates provided in section 3.3 are supported in section 4.1 by convergence tests comprised of solid body rotations about various axes, deformational flows, and compressible flows. The method is shown to be globally second-order accurate for tracer transport independent of the velocity and second-order for the density transport in the incompressible setting and first-order accurate for compressible flows. In addition to these results, the ability to exactly preserve non-linear correlations between advected quantities was illustrated in 9. Unique features of the method include the coherent advection of multiple quantities with a single numerically approximated backward characteristic map and the ability to retain all scales present in the initial condition. In section 4.2.2, we showcased the latter of these features with a zoom-in on the solution for a fractal set in a complex flow environment.

Improving upon the method in its present form offers many interesting avenues of investigation. Given its unique features, a deeper study of the advantages of the CM method for the advection of multiple chemical tracer species in comparison with existing techniques is warranted. Beyond transport on the sphere, the extrinsic formulation presented here permits the application of the method to more general embedded submanifolds. Finally, the method is not limited to the transport of quantities which do not interact with the advecting velocity field. The CM method has been successfully applied to the solution of the incompressible Euler equations on a two dimensional periodic domain using the advection of the vorticity [35]. The extension of these techniques to a spherical geometry and to the solution of the shallow water equations is the subject of our current research. We believe that the CM method offers a unique and useful tool for problems related to geophysical fluid dynamics.

## Declaration of competing interest

The authors declare that they have no known competing financial interests or personal relationships that could have appeared to influence the work reported in this paper.

## Acknowledgments

ST was supported by the NSERC PGS-D program. JCN was supported by the NSERC Discovery Grant program. The authors would like to thank Xi-Yuan Yin of McGill University for many helpful discussions and insights.

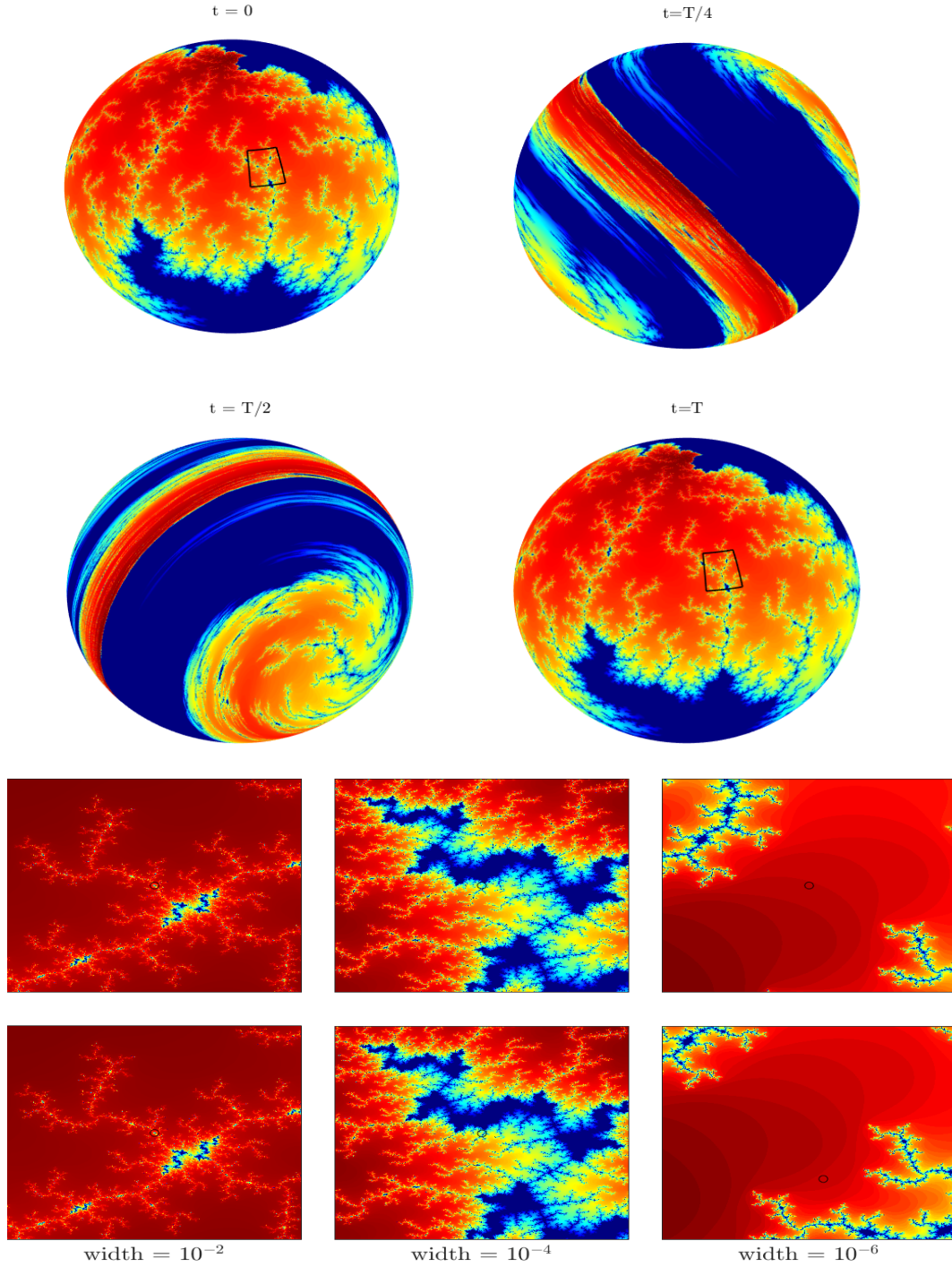


Figure 10: Top: Advection of the Mandelbrot set on the sphere under the velocity field (4.10) with parameters  $\alpha = \pi/4$  and  $T = 5$ . Bottom: Zoom on window depicted at times  $t = 0$  (top row) and  $t = 5$  (bottom row) up to a width of  $10^{-6}$  with focal point given by the black circle.

## References

- [1] J.-F. Lamarque, L. Emmons, P. Hess, D. E. Kinnison, S. Tilmes, F. Vitt, C. Heald, E. A. Holland, P. Lauritzen, J. Neu, et al., Cam-chem: Description and evaluation of interactive atmospheric chemistry in the community earth system model, *Geoscientific Model Development* 5 (2) (2012) 369.

- [2] J.-F. Lamarque, D. Kinnison, P. Hess, F. Vitt, Simulated lower stratospheric trends between 1970 and 2005: Identifying the role of climate and composition changes, *Journal of Geophysical Research: Atmospheres* 113 (D12) (2008).
- [3] J. Thuburn, M. E. McIntyre, Numerical advection schemes, cross-isentropic random walks, and correlations between chemical species, *Journal of Geophysical Research: Atmospheres* 102 (D6) (1997) 6775–6797.
- [4] M. J. Prather, X. Zhu, S. E. Strahan, S. D. Steenrod, J. M. Rodriguez, Quantifying errors in trace species transport modeling, *Proceedings of the National Academy of Sciences* 105 (50) (2008) 19617–19621.
- [5] O. Wild, M. J. Prather, Global tropospheric ozone modeling: Quantifying errors due to grid resolution, *Journal of Geophysical Research: Atmospheres* 111 (D11) (2006).
- [6] M. J. Berger, P. Colella, et al., Local adaptive mesh refinement for shock hydrodynamics, *Journal of computational Physics* 82 (1) (1989) 64–84.
- [7] M. J. Berger, J. Olinger, Adaptive mesh refinement for hyperbolic partial differential equations, *Journal of computational Physics* 53 (3) (1984) 484–512.
- [8] N. Flyer, E. Lehto, Rotational transport on a sphere: Local node refinement with radial basis functions, *Journal of Computational Physics* 229 (6) (2010) 1954–1969.
- [9] A. Staniforth, J. Côté, Semi-lagrangian integration schemes for atmospheric models—a review, *Monthly weather review* 119 (9) (1991) 2206–2223.
- [10] P. Welander, Studies on the general development of motion in a two-dimensional, ideal fluid, *Tellus* 7 (2) (1955) 141–156.
- [11] M. Perlman, On the accuracy of vortex methods, *Journal of Computational Physics* 59 (2) (1985) 200–223.
- [12] L. Barba, A. Leonard, C. Allen, Advances in viscous vortex methods—meshless spatial adaption based on radial basis function interpolation, *International Journal for Numerical Methods in Fluids* 47 (5) (2005) 387–421.
- [13] J. T. Beale, A. Majda, High order accurate vortex methods with explicit velocity kernels, *Journal of Computational Physics* 58 (2) (1985) 188–208.
- [14] A. Magni, G.-H. Cottet, Accurate, non-oscillatory, remeshing schemes for particle methods, *Journal of Computational Physics* 231 (1) (2012) 152–172.
- [15] H. O. Nordmark, Rezoning for higher order vortex methods, *Journal of Computational Physics* 97 (2) (1991) 366–397.
- [16] M. Bergdorf, P. Koumoutsakos, A lagrangian particle-wavelet method, *Multiscale Modeling & Simulation* 5 (3) (2006) 980–995.
- [17] M. Bergdorf, G.-H. Cottet, P. Koumoutsakos, Multilevel adaptive particle methods for convection-diffusion equations, *Multiscale Modeling & Simulation* 4 (1) (2005) 328–357.
- [18] P. A. Bosler, J. Kent, R. Krasny, C. Jablonowski, A lagrangian particle method with remeshing for tracer transport on the sphere, *Journal of Computational Physics* 340 (2017) 639–654.
- [19] P. A. Bosler, Particle methods for geophysical flow on the sphere., Ph.D. thesis (2013).
- [20] P. Bosler, L. Wang, C. Jablonowski, R. Krasny, A lagrangian particle/panel method for the barotropic vorticity equations on a rotating sphere, *Fluid Dynamics Research* 46 (3) (2014) 031406.
- [21] C. W. Hirt, A. A. Amsden, J. Cook, An arbitrary lagrangian-eulerian computing method for all flow speeds, *Journal of computational physics* 14 (3) (1974) 227–253.
- [22] C. Cotter, J. Frank, S. Reich, The remapped particle-mesh semi-lagrangian advection scheme, *Quarterly Journal of the Royal Meteorological Society: A journal of the atmospheric sciences, applied meteorology and physical oceanography* 133 (622) (2007) 251–260.
- [23] G.-H. Cottet, J.-M. Etancelin, F. Pérignon, C. Picard, High order semi-lagrangian particle methods for transport equations: numerical analysis and implementation issues, *ESAIM: Mathematical Modelling and Numerical Analysis* 48 (4) (2014) 1029–1060.
- [24] S.-J. Lin, R. B. Rood, Multidimensional flux-form semi-lagrangian transport schemes, *Monthly Weather Review* 124 (9) (1996) 2046–2070.
- [25] E. Kaas, B. Sørensen, P. H. Lauritzen, A. B. Hansen, A hybrid eulerian–lagrangian numerical scheme for solving prognostic equations in fluid dynamics, *Geoscientific Model Development* 6 (6) (2013) 2023–2047.
- [26] J. Xiao, L. Wang, J. P. Boyd, Rbf-vortex methods for the barotropic vorticity equation on a sphere, *Journal of Computational Physics* 285 (2015) 208–225.

- [27] V. Shankar, G. B. Wright, Mesh-free semi-lagrangian methods for transport on a sphere using radial basis functions, *Journal of Computational Physics* 366 (2018) 170–190.
- [28] P. H. Lauritzen, R. D. Nair, P. A. Ullrich, A conservative semi-lagrangian multi-tracer transport scheme (cslam) on the cubed-sphere grid, *Journal of Computational Physics* 229 (5) (2010) 1401–1424.
- [29] L. M. Harris, P. H. Lauritzen, R. Mittal, A flux-form version of the conservative semi-lagrangian multi-tracer transport scheme (cslam) on the cubed sphere grid, *Journal of Computational Physics* 230 (4) (2011) 1215–1237.
- [30] S. Osher, R. Fedkiw, K. Piechor, Level set methods and dynamic implicit surfaces, *Appl. Mech. Rev.* 57 (3) (2004) B15–B15.
- [31] B. Seibold, R. R. Rosales, J.-C. Nave, Jet schemes for advection problems, *Discrete & Continuous Dynamical Systems - B* 17 (2012) 1229. doi:10.3934/dcdsb.2012.17.1229.
- [32] J.-C. Nave, R. R. Rosales, B. Seibold, A gradient-augmented level set method with an optimally local, coherent advection scheme, *Journal of Computational Physics* 229 (10) (2010) 3802–3827.
- [33] H. Kohn, J.-C. Nave, A new method for the level set equation using a hierarchical-gradient truncation and remapping technique, *Computer Physics Communications* 184 (6) (2013) 1547–1554.
- [34] O. Mercier, X.-Y. Yin, J.-C. Nave, The characteristic mapping method for the linear advection of arbitrary sets, *SIAM Journal on Scientific Computing* 42 (3) (2020) A1663–A1685.
- [35] X.-Y. Yin, O. Mercier, B. Yadav, K. Schneider, J.-C. Nave, A characteristic mapping method for the two-dimensional incompressible euler equations, *Journal of Computational Physics* 424 (2021) 109781.
- [36] X.-Y. Yin, K. Schneider, J.-C. Nave, A characteristic mapping method for the three-dimensional incompressible euler equations, *arXiv preprint arXiv:2107.03504* (2021).
- [37] R. D. Nair, P. H. Lauritzen, A class of deformational flow test cases for linear transport problems on the sphere, *Journal of Computational Physics* 229 (23) (2010) 8868–8887.
- [38] A. Kageyama, T. Sato, “yin-yang grid”: An overset grid in spherical geometry, *Geochemistry, Geophysics, Geosystems* 5 (9) (2004).
- [39] E. S. Gawlik, M. Leok, Embedding-based interpolation on the special orthogonal group, *SIAM Journal on Scientific Computing* 40 (2) (2018) A721–A746.
- [40] P. Grohs, H. Hardering, O. Sander, M. Sprecher, Projection-based finite elements for nonlinear function spaces, *SIAM Journal on Numerical Analysis* 57 (1) (2019) 404–428.
- [41] M.-J. Lai, L. L. Schumaker, *Spline functions on triangulations*, Vol. 110, Cambridge University Press, 2007.
- [42] P. Alfeld, M. Neamtu, L. L. Schumaker, Fitting scattered data on sphere-like surfaces using spherical splines, *Journal of Computational and Applied Mathematics* 73 (1) (1996) 5–43.
- [43] P. Alfeld, M. Neamtu, L. L. Schumaker, Dimension and local bases of homogeneous spline spaces, *SIAM Journal on Mathematical Analysis* 27 (5) (1996) 1482–1501.
- [44] P. Alfeld, M. Neamtu, L. L. Schumaker, Bernstein-bézier polynomials on spheres and sphere-like surfaces, *Computer Aided Geometric Design* 13 (4) (1996) 333–349.
- [45] M. J. Powell, M. A. Sabin, Piecewise quadratic approximations on triangles, *ACM Transactions on Mathematical Software (TOMS)* 3 (4) (1977) 316–325.
- [46] L. L. Schumaker, *Spline functions: computational methods*, SIAM, 2015.
- [47] O. Davydov, L. L. Schumaker, Interpolation and scattered data fitting on manifolds using projected powell-sabin splines, *IMA journal of numerical analysis* 28 (4) (2008) 785–805.
- [48] R. Hielscher, L. Lippert, Approximating the derivative of manifold-valued functions, *arXiv preprint arXiv:2102.12562* (2021).
- [49] H. Munthe-Kaas, Runge-kutta methods on lie groups, *BIT Numerical Mathematics* 38 (1) (1998) 92–111.
- [50] D. Lewis, N. Nigam, Geometric integration on spheres and some interesting applications, *Journal of Computational and Applied Mathematics* 151 (1) (2003) 141–170.
- [51] A. Iserles, H. Z. Munthe-Kaas, S. P. Nørsett, A. Zanna, Lie-group methods, *Acta numerica* 9 (2000) 215–365.
- [52] E. Hairer, C. Lubich, G. Wanner, Structure-preserving algorithms for ordinary differential equations, *Geometric numerical integration* 31 (2006).

- [53] X.-Y. Yin, L. Chen, J.-C. Nave, A diffusion-driven characteristic mapping method for particle management, *SIAM Journal on Scientific Computing* 43 (5) (2021) A3155–A3183.
- [54] R. D. Nair, C. Jablonowski, Moving vortices on the sphere: A test case for horizontal advection problems, *Monthly Weather Review* 136 (2) (2008) 699–711.
- [55] L. Moresi, B. Mather, Stripy: A python module for (constrained) triangulation in cartesian coordinates and on a sphere., *Journal of Open Source Software* 4 (38) (2019) 1410.
- [56] R. J. Renka, Algorithm 772: Stripack: Delaunay triangulation and voronoi diagram on the surface of a sphere, *ACM Transactions on Mathematical Software (TOMS)* 23 (3) (1997) 416–434.
- [57] A. Jacobson, D. Panozzo, et al., libigl: A simple C++ geometry processing library, <https://libigl.github.io/> (2018).
- [58] J. R. Baumgardner, P. O. Frederickson, Icosahedral discretization of the two-sphere, *SIAM Journal on Numerical Analysis* 22 (6) (1985) 1107–1115.
- [59] S. T. Zalesak, Fully multidimensional flux-corrected transport algorithms for fluids, *Journal of computational physics* 31 (3) (1979) 335–362.
- [60] R. Nair, J. Côté, A. Staniforth, Cascade interpolation for semi-lagrangian advection over the sphere, *Quarterly Journal of the Royal Meteorological Society* 125 (556) (1999) 1445–1468.
- [61] R. D. Nair, B. Machenhauer, The mass-conservative cell-integrated semi-lagrangian advection scheme on the sphere, *Monthly Weather Review* 130 (3) (2002) 649–667.
- [62] P. H. Lauritzen, J. Thuburn, Evaluating advection/transport schemes using interrelated tracers, scatter plots and numerical mixing diagnostics, *Quarterly Journal of the Royal Meteorological Society* 138 (665) (2012) 906–918.